Monthly Notices of the ROYAL ASTRONOMICAL SOCIETY

MNRAS **484,** 2587–2604 (2019) doi:10.1093/mnras/sty3323
Advance Access publication 2018 December 7

Supernova dust yields: the role of metallicity, rotation, and fallback

S. Marassi,[1]★ R. Schneider,[1,2,3] M. Limongi,[1,3] A. Chieffi,[4,5] L. Graziani[1] and S. Bianchi[6]

[1]*INAF/Osservatorio Astronomico di Roma, Via di Frascati 33, I-00040 Monte Porzio Catone, Italy*
[2]*Dipartimento di Fisica, 'Sapienza' Università di Roma, Piazzale Aldo Moro 5, I-00185 Roma, Italy*
[3]*Kavli Institute for the Physics and Mathematics of the Universe, Todai Institutes for Advanced Study, the University of Tokyo, Kashiwa 277-8583, Japan*
[4]*INAF/IAPS, Via Fosso del Cavaliere 100, I-00133 Roma, Italy*
[5]*Monash Centre for Astrophysics (MoCA), School of Mathematical Sciences, Monash University, Victoria 3800, Australia*
[6]*INAF/Osservatorio Astrofisico di Arcetri, Largo E. Fermi 5, I-50125 Firenze, Italy*

Accepted 2018 November 27. Received 2018 November 26; in original form 2017 December 14

ABSTRACT

Supernovae (SNe) are considered to have a major role in dust enrichment of high-redshift galaxies and, due to the short lifetimes of interstellar grains, in dust replenishment of local galaxies. Here we explore how SN dust yields depend on the mass, metallicity, and rotation rate of the progenitor stars, and on the properties of the explosion. To this aim, assuming uniform mixing inside the ejecta, we quantify the dust mass produced by a sample of SN models with progenitor masses $13\,M_{\odot} \leq M \leq 120\,M_{\odot}$, metallicity $-3 \leq [Fe/H] \leq 0$, rotation rate $v_{rot} = 0$, and 300 km s^{-1}, that explode with a fixed energy of 1.2×10^{51} erg (FE models) or with explosion properties calibrated to reproduce the ^{56}Ni–M relation inferred from SN observations (CE models). We find that rotation favours more efficient dust production, particularly for more massive, low-metallicity stars, but that metallicity and explosion properties have the largest effects on the dust mass and its composition. In FE models, SNe with $M \leq 20-25\,M_{\odot}$ are more efficient at forming dust: between 0.1 and 1 $M_{\odot}$ is formed in a single explosion, with a composition dominated by silicates, carbon, and magnetite grains when [Fe/H] = 0, and by carbon and magnetite grains when [Fe/H] < 0. In CE models, the ejecta are massive and metal-rich and dust production is more efficient. The dust mass increases with M and it is dominated by silicates, at all [Fe/H].

Key words: stars: abundances – stars: evolution – supernovae: general – ISM: abundances – dust, extinction – galaxies: ISM.

1 INTRODUCTION

Dust in astrophysical environments has an important role as it regulates the physical and chemical conditions in the interstellar medium (ISM). Expanding ejecta of core-collapse supernovae (SNe) are possible sites of dust formation. Knowledge of the dust mass condensed in SN explosions and injected in the ISM is of primary importance for the understanding of early dust enrichment in galaxies (Dayal & Ferrara 2018).

Infrared (IR) and submillimeter (submm) data obtained using different space and ground-based telescopes (*Spitzer*, *Herschel*, SOFIA, AKARI, and ALMA) have provided strong evidence of dust formation in the ejecta of SN remnants in the Milky Way and the Large Magellanic Cloud (Dunne et al. 2009; Barlow et al. 2010; Otsuka et al. 2010; Matsuura et al. 2011; Gomez et al. 2012; Temim et al. 2015, 2017; De Looze et al. 2017). Newly formed dust masses in SNe in more distant galaxies have been recently inferred through the modelling of the blue–red asymmetries of late-time optical and near-IR line profiles (SN1980K and SN1993J; Bevan, Barlow & Milisavljevic 2017). The masses of cold dust inferred from far-IR and submm observations span a large range of values, from 0.1 $M_{\odot}$ of cool dust in Cas A (Barlow et al. 2010, but see the recent upward revision by De Looze et al. 2017, who estimate $0.3-0.6\,M_{\odot}$ of silicate/carbon grains) to $(0.4-0.7)\,M_{\odot}$ in SN1987A (Matsuura et al. 2011, 2015; Indebetouw et al. 2014; Bevan & Barlow 2016) and the minimum estimated dust mass of $\gtrsim 0.3\,M_{\odot}$ for SNR G54.1+0.3 (Rho et al. 2017; Temim et al. 2017). For a discussion on the dependence of dust formation on the progenitor mass and supernova type we refer to the review by Gall, Hjorth & Andersen (2011).

Theoretical models have attempted to predict the amount of freshly formed dust in SN ejecta adopting nucleation theory (Kozasa, Hasegawa & Nomoto 1991; Todini & Ferrara 2001;

★ E-mail: stefania.marassi@roma1.infn.it

Nozawa et al. 2003, 2010; Schneider, Ferrara & Salvaterra 2004; Bianchi & Schneider 2007; Marassi et al. 2015; Lazzati & Heger 2016) or a kinetic approach (Cherchneff & Dwek 2009, 2010), including a description of grain growth (Sarangi & Cherchneff 2013, 2015), and coagulation (Sluder, Milosavljević & Montgomery 2018). We refer the interested reader to Marassi et al. (2015) for a discussion of the differences between the two approaches.

Classical nucleation theory (CNT) has proven to be suitable to follow dust condensation in SN ejecta (Nozawa & Kozasa 2013; Nozawa et al. 2015), despite its dependence on parameters, such as the sticking coefficient or the minimum number of monomers forming the first seed nuclei (Bianchi & Schneider 2007). Grids of SN dust yields have been computed using CNT starting from different set of progenitors and SN explosion models. Todini & Ferrara (2001) and Bianchi & Schneider (2007) have considered SN progenitors with masses in the range $[12-35]\,M_{\odot}$ and metallicity values in the range [0–1] $Z_{\odot}$ using Woosley & Weaver (1995) SN models. Nozawa et al. (2003) built a grid of dust yields for Pop III core-collapse SNe with metal-free progenitors in the mass range [13–30] $M_{\odot}$ and for Pop III pair instability SNe (PISNe) with stellar progenitors masses of 170 and 200 $M_{\odot}$. For all these cases they adopted the SN explosion and nucleosynthesis calculations of Umeda & Nomoto (2002). Schneider et al. (2004) have considered the nucleation of dust in the ejecta of Pop III PISNe with progenitor masses in the range [140–260] $M_{\odot}$ using the grid of PISN models by Heger & Woosley (2002). More recently, Marassi et al. (2015) have used an improved version of the Bianchi & Schneider (2007) model to estimate the dust yields of *standard* and *faint* Pop III SNe, starting from a homogeneous set of pre-supernova models with progenitor masses in the range [13–80] $M_{\odot}$ (Limongi & Chieffi 2012) and varying the degree of mixing and fallback during the explosion.

The above studies consistently show that the composition, size distribution, and total mass of dust formed in the ejecta depend on the physical properties of the stellar progenitors (mass and metallicity), on the explosion energy, and on the ejecta temperature and density profiles (Todini & Ferrara 2001; Nozawa et al. 2003, 2010; Schneider et al. 2004; Bianchi & Schneider 2007; Cherchneff & Dwek 2009, 2010; Kozasa et al. 2009; Sarangi & Cherchneff 2013, 2015; Marassi et al. 2015). However, none of these studies have explored the effects of stellar rotation on the dust mass formed in the ejecta. In fact, many stellar evolutionary processes are affected by rotation and this is reflected in the properties of the star at the pre-SN stage (see e.g. Chieffi & Limongi 2017; Limongi 2017). Finally, the physical properties of the ejecta depend on the supernova type (Nozawa et al. 2010). The most commonly observed dusty SNe are core-collapse Type II-P, but there are evidence of dust formation also in SN type IIb and Ib (Gall et al. 2011). Conversely, dust grains formed in the ejecta of SNe Ia are almost completely destroyed in the shocked gas before being injected into the ISM (Nozawa et al. 2011).

The composition and size distribution of grains formed in SN ejecta a few hundred days after the explosions are critical information to estimate the dust mass that survives the subsequent passage of the reverse shock on time-scales of 10^3 and 10^5 yr and effectively enrich the ISM (Bianchi & Schneider 2007; Nozawa et al. 2007; Silvia, Smith & Shull 2010, 2012; Biscaro & Cherchneff 2014, 2016; Marassi et al. 2014; Bocchio et al. 2016; Micelotta, Dwek & Slavin 2016). With the exception of SN 1987A, which is too young for the reverse shock to have affected the dust mass, theoretical models suggest that the dust mass currently observed in SN remnants is only a fraction (ranging between 60 and 90 per cent) of the initial dust mass formed in the explosion (Bocchio et al. 2016), in agreement with the observational evidence for ongoing dust destruction in Cas A (Barlow et al. 2010).

The goal of this study is to provide a tabulated set of dust masses that takes into account the great diversity of SN events, spanning a large range of progenitor masses and metallicity. We study the dependence of the mass of dust on metallicity, rotation, and fallback, to assess the relative importance of these processes on dust formation. Although mass-loss can be significant, especially at solar metallicity, we do not consider dust formation in stellar winds and we restrict our analysis to dust formation in SN ejecta. Having this goal in mind, we investigate two samples of SN models: a *fixed* energy sample (hereafter FE models) and a *calibrated* explosion sample (hereafter CE models). The first sample is made by SN progenitor masses in the range [13–120] $M_{\odot}$ that explode with a fixed energy of 1.2×10^{51} erg (Limongi & Chieffi 2018). This is divided in two subdata set that differ for the adopted rotation degree: non-rotating (NR) and rotating (ROT) progenitors models with initial equatorial rotational velocities of $v = 0$ and $v = 300$ km s^{-1}, respectively. These values are meant to provide a minimum and maximum estimate of the impact of rotation as they bracket the bulk of the observed rotation velocities in the Milky Way (Dufton et al. 2006), and in SMC/LMC (Hunter et al. 2008; Ramírez-Agudelo et al. 2017). In turn, each sub-data set contains four different classes of progenitor metallicity: class 0 ([Fe/H] = 0), −1 ([Fe/H] = −1), −2 ([Fe/H] = −2), and −3 ([Fe/H] = −3). In the second sample, CE models have the same structure of FE models but their explosion energy is not fixed a priori. Rather, its value is calibrated requiring that the exploding SNe eject the entire stellar mantle (Limongi 2017).

With this choice, we can perform a *parametric* study to investigate how metallicity, rotation, and fallback impact (*i*) the nucleosynthetic output of the explosion, and (*ii*) the total mass, size, and composition of dust formed in the ejecta. All the SN dust yields are available upon request.

The paper is organized as follows. In Section 2, we describe the two samples of FE and CE SN models. For each of these, in Section 3, we discuss the most important properties, such as the masses of the stellar remnants and the ejecta metal composition, as a function of rotation and metallicity. In Section 4, we briefly recall the main features of the adopted dust formation model (Bianchi & Schneider 2007; Marassi et al. 2015). In Section 5, we discuss the dust masses obtained for the FE and CE samples. Finally, in Section 6, we draw our main conclusions.

2 CALIBRATION OF SN MODELS

SNe show large differences in physical properties, and their final outcome depends on the mass, metallicity, rotation, and mass-loss rate of their progenitors (see e.g. Smartt 2009; Limongi 2017 and references therein). One possible choice to construct a reference sample is to assign the explosion energy and vary the progenitor mass and metallicity, as done by Woosley & Weaver (1995). On the other hand, the observed SNe exhibit a range of explosion energies. Fig. 1 shows a collection of data where the main-sequence progenitor mass and the ^{56}Ni mass have been estimated comparing theoretical and observed light curves (Nomoto, Kobayashi & Tominaga 2013). The data span a large variety of SNe, ranging from hypernovae (red data points) to faint SNe (orange data points). As an attempt to account for this diversity of objects we decided to adopt two different SN reference samples.

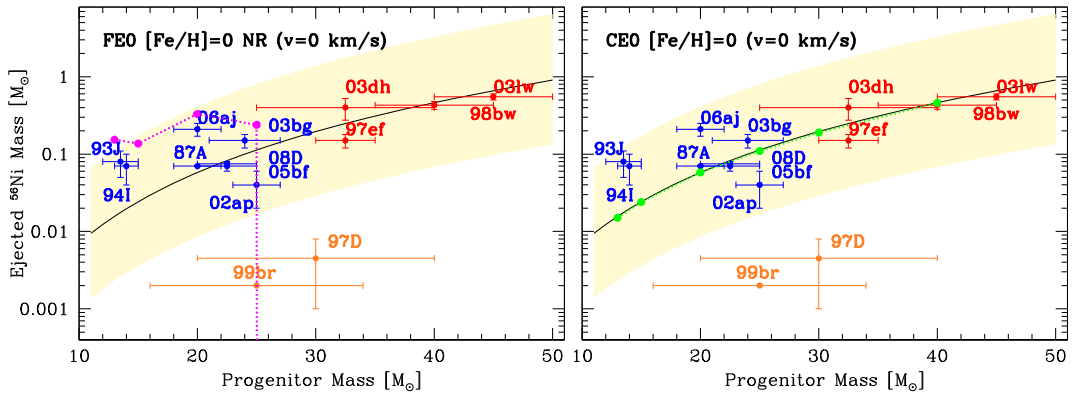

Figure 1. Ejected ^{56}Ni mass as a function of the main-sequence mass of the progenitors for several SNe (normal SNe in blue, hypernovae in red, and faint SNe in orange). Data are from Nomoto et al. (2013). The black curve is the best fit to the data. *Left-hand panel*: the dashed magenta line with points shows the prediction of FE, solar metallicity, NR models. *Right-hand panel*: the green solid line with points shows the prediction of CE, solar metallicity, NR models after the calibration procedure.

The first sample comprises SN progenitors with masses in the range [13–120] $M_\odot$ which explode with a fixed energy of 1.2×10^{51} ergs (FE models). This sample is divided in two additional sub-set: NR models ($v = 0$) and ROT models ($v = 300$ km s^{-1}). Depending on the SN progenitor metallicity, each sub-set contains four different classes: class FE0 (FE, [Fe/H] = 0), FE-1 (FE, [Fe/H] = −1), FE-2 (FE, [Fe/H] = −2), and FE-3 (FE, [Fe/H] = −3). The FE sample allows us to understand how metallicity and rotation affect both the fallback (hence the mass of the stellar remnant) and the physical properties of the ejecta, such as its mass and chemical composition.

In the left-hand panel of Fig. 1, we show the ^{56}Ni mass ejected by solar FE NR models (FE0-NR SNe, dashed magenta line with points): in these SN models, the ejection of ^{56}Ni occurs only in low-mass progenitors. These models are not able to reproduce the larger ^{56}Ni masses ejected by hypernovae with $> 30\,M_\odot$ progenitors. Rotation does not alter this conclusion because in solar FE ROT models (FE0-ROT SNe) only the 13 and 15 $M_\odot$ progenitor models eject a non-zero ^{56}Ni mass (see Table 5). Besides, observations show that the same SN types do not eject the same amount of ^{56}Ni mass (Hamuy 2003; Nomoto et al. 2013). As an example, the blue data points encompass a factor of 10 in nichel masses (shaded yellow region in Fig. 1; Hamuy 2003).

For these reasons, we considered a second sample of SN models which spans the same range of progenitor masses of FE models, [13–120] $M_\odot$, but the properties of the explosions are calibrated to reproduce the amount of ^{56}Ni obtained from the best fit to the observations, as shown by the black line in the right-hand panel of Fig. 1 (CE models). 1D simulations, in the framework of the kinetic bomb, require that the initial velocity is tuned in some way to get a successful explosion, e.g. to obtain a given value for the final kinetic energy. In CE progenitor models, on the other hand, the initial velocity is taken as the minimum initial velocity which provides the ejection of the whole mantle above the iron core (see Chieffi & Limongi 2013 for further details). As explained in Chieffi & Limongi (2013), this approach allows to choose the mass cut (i.e., the mass coordinate which separates the SN ejecta from the compact remnant) a-posteriori and to calibrate the model by requiring the ejection of a specific amount of ^{56}Ni. This procedure has been tested and does not alter significantly the final yields (Chieffi & Limongi 2003). The structure of the CE sample is the same as that of FE models: it is divided in two additional sub-set, NR/ROT models, and each sub-set contains four different classes, depending on the progenitor metallicity: set CE0 (CE, [Fe/H] = 0), set CE-1 (CE, [Fe/H] = −1), set CE-2 (CE, [Fe/H] = −2), and set CE-3 (CE, [Fe/H] = −3). The same observed best-fitting ^{56}Ni – progenitor mass relation is adopted to calibrate models with different metallicity values and rotation rates, due to the limitations of available observations.

It should be noted that the ^{56}Ni mass and the progenitor mass reported in Fig. 1 for the observed SN sample have been derived using theoretical models (Nomoto et al. 2013). As an example, in type II-P SNe (as e.g. SN1987A in Fig. 1), the ^{56}Ni mass is derived from the brightness of the SN exponential tails, assuming that all the gamma-rays due to decay of ^{56}Co → ^{56}Fe are fully thermalized (Hamuy 2003). The uncertainties/approximations of this approach are quantified by the errors on the estimated ^{56}Ni and stellar progenitor masses.

3 PROPERTIES OF SN MODELS

In this section, we discuss some of the most important physical properties of the SN models. Both FE and CE samples are simulated with the latest version of the FRANEC code which takes into account the effects of rotation and metallicity on the evolution of the star (for more details see Chieffi & Limongi 2013 and Limongi & Chieffi 2018).

Hachinger et al. (2012) classify core-collapse SN models depending on H and He envelope masses in the pre-supernova phase. In particular, they set (i) the minimum H mass for a type II-P SN to be $M(\mathrm{H})_{\mathrm{min,SNIIP}} \simeq 0.3\,M_\odot$; (ii) the H mass for a type IIb SN to be $0.1 M_\odot \lesssim M(\mathrm{H})_{\mathrm{SNIIb}} \lesssim 0.3\,M_\odot$; (iii) when the H mass is $\lesssim 0.1\,M_\odot$, the SN is classified as a type Ib if $M(\mathrm{He}) \gtrsim 0.1\,M_\odot$ or as a type Ic if $M(\mathrm{He}) \lesssim 0.1\,M_\odot$. We adopt the same classification here (see also Chieffi & Limongi 2013 and Limongi 2017) and, for each model, the inferred SN type is shown in Tables 1–12. We find that none of the SN models in our CE and FE samples can be classified as a SNIc. This is a consequence of the rather high-He mass present in the envelope at the time of the explosion (Limongi 2017). The lack of SNIc is irrelevant for dust production as Hunter et al. (2009) found no evidence of dust condensation in the ejecta of the prototypical Ic SN 2007gr and this class of SNe is not considered to be an important source of dust (Gall et al. 2011).

The mass of dust formed in the ejecta depends on the metal abundances and on their distribution. Fig. 2 illustrates the variety of

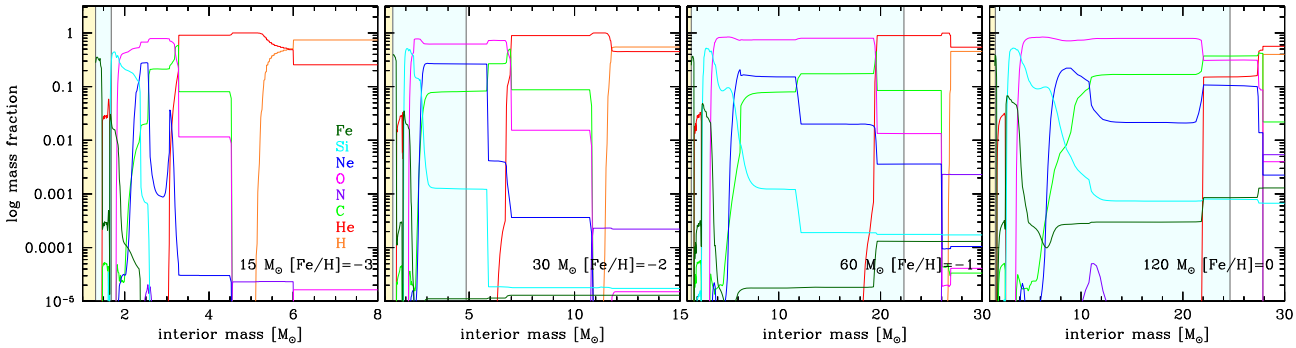

Figure 2. Pre-supernova chemical structure for four selected NR models. From left to right: 15 $M_\odot$ with [Fe/H] = −3, 30 $M_\odot$ with [Fe/H] = −2, 60 $M_\odot$ with [Fe/H] = −1, and 120 $M_\odot$ with [Fe/H] = 0. Different coloured shaded regions indicate the remnant mass for CE (yellow) and FE (azure) models. A colour version of the figure is available online.

chemical compositions that characterize the pre-supernova models. The mass fraction profiles for the most abundant atomic elements are shown for four selected models at different metallicity: 15 $M_\odot$ with [Fe/H] = −3, 30 $M_\odot$ with [Fe/H] = −2, 60 $M_\odot$ with [Fe/H] = −1 and 120 $M_\odot$ with [Fe/H] = 0. In addition, in each panel we also show the range of pre-SN mass that collapses and forms the remnant for FE and CE SN models (azure and yellow shaded regions, respectively). For the 15 $M_\odot$ pre-SN, the remnant mass is always 1.3 $M_\odot$ (azure and yellow regions are superimposed in the right-hand panel). When the progenitor mass increases, fallback and remnant mass increase in FE models, resulting in smaller and more metal-poor ejecta compared to the corresponding CE models.[1] As a result, FE and CE models place a lower and upper limit on the dust mass that forms in our grid of SN models. In the following subsections, we discuss the effects of metallicity and rotation on FE and CE SN models.

3.1 FE models

We first analyse the effects of metallicity on the NR FE models. The leftmost panel of Fig. 3 shows that the remnant mass increases with progenitor mass and with decreasing metallicity. This is due to the increasing compactness and smaller mass-loss experienced by stars at lower metallicity. As a consequence, not all these models lead to a successful explosion: stars with $M > 40\,M_\odot$ in set FE-2 and with $M > 30\,M_\odot$ in set FE-3 undergo a huge fallback and end their life as a failed SN event, forming a black hole. Since these models loose only a small fraction of their H-envelope before collapsing to a black hole, they do not contribute to metal and dust enrichment (we only report their pre-SN and final remnant masses in Tables 3 and 4). In addition, when [Fe/H] ≤ -1 the most massive progenitors, with $M > 80\,M_\odot$, enter the pulsation pair instability regime (Heger & Woosley 2002) and their final fate cannot be computed with precision in this framework. For this reason, these models are not shown in the figure and in the corresponding tables.

The effect of rotation on the evolution of massive stars is twofold: *(i)* rotation driven mixing leads to more massive CO cores, and *(ii)* rotation favours a more efficient mass-loss that in turn, in the most extreme cases, may induce a reduction of the CO core masses.[2] The interplay between these two different effects determines the final remnant mass, because (for a fixed explosion energy) this quantity directly depends on the CO core mass at the time of the explosion.

At solar metallicity, the increase of the CO core mass is the dominant effect for stars with $M < 40\,M_\odot$. At larger stellar masses, the more efficient mass-loss is the dominant effect. As a consequence, when compared to NR models, the remnant mass of ROT models with [Fe/H] = 0 increases for stars with $M < 40\,M_\odot$ and decreases for stars with $M > 40\,M_\odot$. A similar behaviour is found for models with [Fe/H] = −1. At lower metallicity, due to the strong reduction of mass-loss, rotation always increases the CO core mass. Therefore, all ROT models with [Fe/H] <-1 lead to more massive remnants than their NR counterparts. Because of the more massive CO cores, the minimum stellar mass that enters the pulsation pair instability reduces if rotation is taken into account. A comparison between the left-hand and the right-hand panel of Fig. 3 clearly shows such a general behavior (see also Tables 1–4).

The metallicity and elemental composition of the ejecta are very important for dust formation. Figs 4 and 5 show the initial metal abundances in the ejecta (prior to dust production) as a function of the progenitor stellar mass for the four metallicity data set, comparing ROT and NR FE models.

The most abundant metals in the ejecta are O and C. In general, for smaller progenitor masses, O > C. When [Fe/H] ≥ -1 (set FE0 and FE-1), there is a progenitor mass above which O < C. At lower metallicity (with the exception of FE-3-NR), oxygen remains the most abundant element, even for very large progenitor masses.

The abundance of heavier and more internal elements is very sensitive to the degree of fallback and rotational mixing. As a result, the mass of Mg, Si, and Fe does not show a simple monotonic trend with progenitor mass (for masses $\leq$ 25–30 $M_\odot$), independently of metallicity and rotation. When [Fe/H] ≥ -1 (set FE0 and FE-1), more massive progenitors have Mg, Si, and Fe abundances that slowly increase with progenitor mass. Due to their massive remnants, the ejecta of massive ROT models at lower metallicity are largely dominated by O, C, and Mg.

An interesting consequence of the dependence of light and heavy element abundances on stellar mass, metallicity, and rotation is the

[1] We assume uniform mixing to take place during the earliest phases of ejecta propagation, hence beyond the mass cut, outside the shaded regions.

[2] The CO core is never directly eroded by mass-loss. Rather, mass-loss can be strong enough to reduce the He core mass and the star develops a smaller CO core.

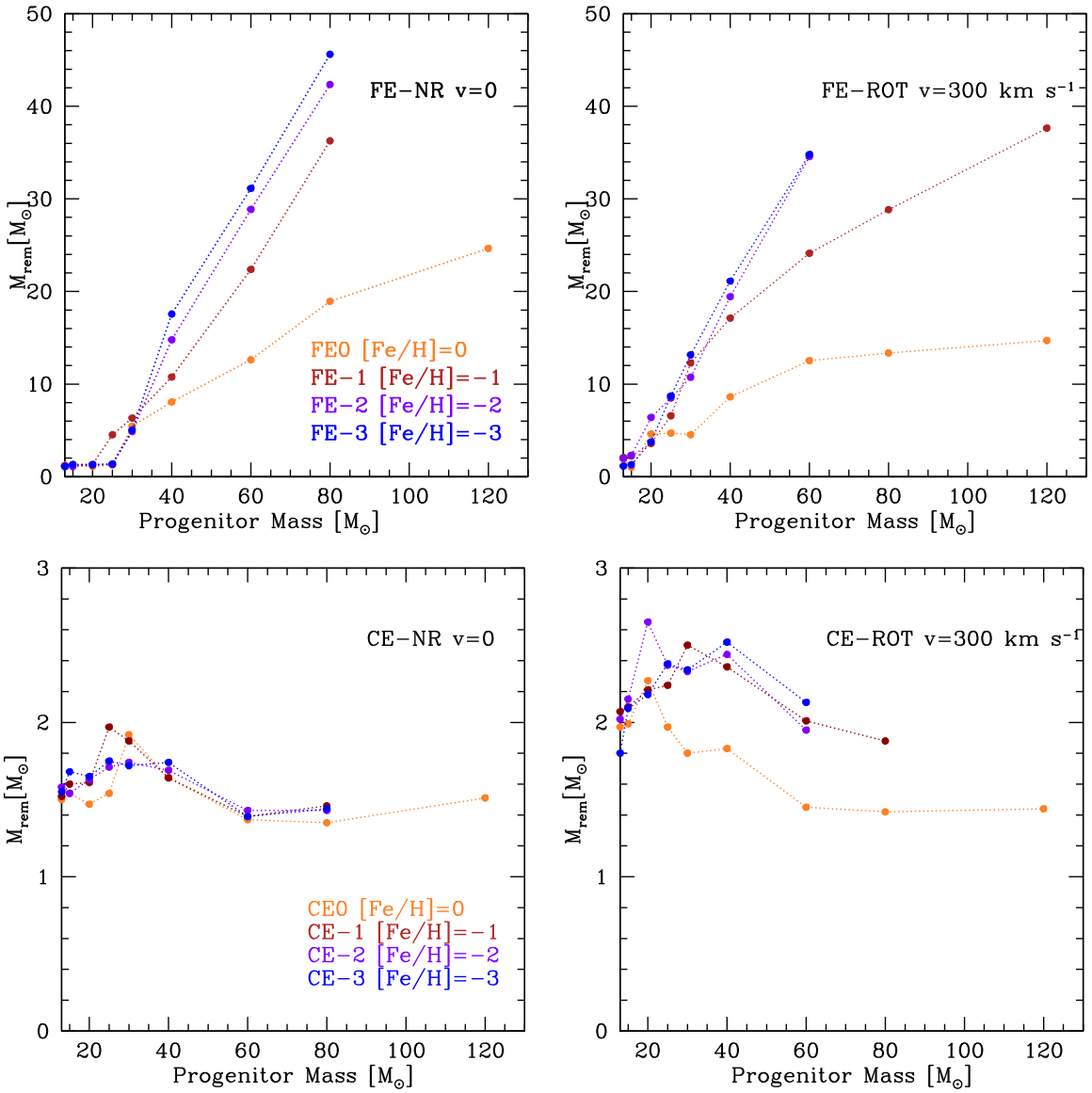

Figure 3. The mass of the remnant as a function of the initial stellar progenitor mass for different metallicity (see the legenda). Upper panels show FE models, lower panels show CE models, and left-hand and right-hand panels show NR and ROT models, respectively.

different degree of [C/Fe] in the ejecta. Using the initial abundances of C ad Fe represented by the light and dark green lines in Figs 4 and 5, we compute [C/Fe] for all FE models and we show it in Fig. 6 as a function of the remnant mass. As expected, [C/Fe] is a strong function of metallicity: for [Fe/H] ≥ -1 (set FE0 and FE-1), [C/Fe] ranges from 0 to ∼2.5, whereas for smaller metallicity (set FE-2 and FE-3), [C/Fe] increases up to ∼3.5–4.5. FE SN models that leave low-mass remnants, with $M_{\rm rem} \lesssim 5\,{\rm M}_{\odot}$, are characterized by [C/Fe] $\lesssim 1$, independently of metallicity and rotation. However, the ejecta of FE SN models that leave more massive remnants are all carbon-enhanced, particularly if the progenitor stars have low initial metallicity and rotate. Indeed, massive, metal-free faint SNe (with mixing and fallback) have been invoked to explain the observed [C/Fe] in carbon-enhanced extremely metal-poor stars, the so-called CEMP-no stars, with [C/Fe] > 0.7 and no traces of rapid or slow neutron capture elements (Beers & Christlieb 2005). Indeed, their peculiar properties have been interpreted as due to the inprints of metal-free SNe (de Bennassuti et al. 2014, 2015) that evolve as faint SNe (Bonifacio, Limongi & Chieffi 2003; Limongi, Chieffi & Bonifacio 2003; Iwamoto et al. 2005; Marassi et al. 2014), or of primordial 'spinstars', which experienced mixing and mass-loss because of their high rotational velocities (Meynet, Ekström & Maeder 2006; Maeder & Meynet 2015). The results shown in Fig. 6 suggest a dependence on metallicity that may have interesting observable implications.

3.2 CE models

The two lower panels in Fig. 3 show the remnant mass as a function of the progenitor mass for CE models. As a consequence of the calibration procedure described in Section 2, the effects of fallback are substantially reduced in CE SN models. The resulting remnants are formed with very similar masses (particularly for NR models) and are much smaller than in FE models, with $1\,{\rm M}_{\odot} \lesssim M_{\rm rem} \lesssim 2\,{\rm M}_{\odot}$. In CE models, the ejecta composition is sensitive to the mass cut, which is chosen to obtain a ^{56}Ni mass in accordance to the

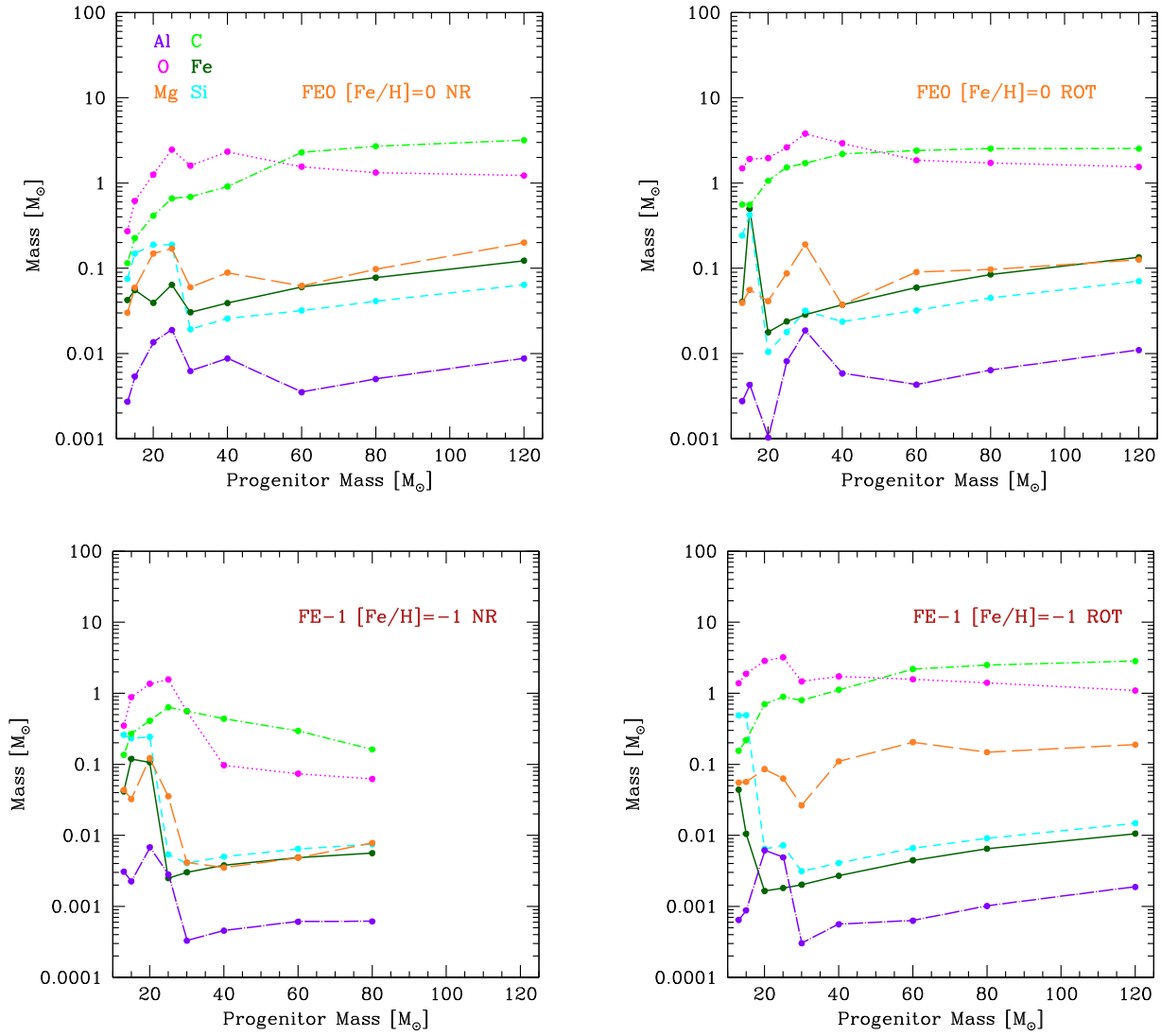

Figure 4. Initial C, O, Mg, Si, Al, and Fe elemental abundances in the ejecta (see the legenda) as a function of the progenitor mass for FE–SN models. Each pair of panels shows a different initial value of metallicity: set FE0 (top left), set FE-1 (bottom left). In each pair, left-hand and right-hand panels show NR and ROT models.

fit described in Section 2. The resulting C, O, Mg, Si, Al, and Fe abundances as a function of the progenitor mass are shown in Fig. 7 for ROT and NR models with different initial metallicity. The ejecta composition is almost independent of metallicity and rotation, because the abundances of metals in the He core are very similar for progenitors with similar mass. The main differences are due to the progenitor mass and to rotation, which induces efficient mixing and affect the abundances of heavier elements (Mg, Si, Al, and Fe), particularly for low-mass progenitors.

4 DUST FORMATION MODEL

The calculation of dust formation in the ejecta is based on CNT. A similar approach has been adopted to investigate dust formation in core-collapse (Todini & Ferrara 2001; Bianchi & Schneider 2007), pair-instability (Schneider et al. 2004), Pop III core collapse (Marassi et al. 2015), and faint SNe (Marassi et al. 2014). The current version of the model is described in Marassi et al. (2015) and it is an improved version of the model adopted by Bianchi & Schneider (2007). Here we briefly summarize the main features of the model and we refer the interested reader to the original papers for more details.

We assume that dust seed clusters are made of $\mathcal{N} \geq 2$ monomers and that the sticking coefficient (defined as the probability that an atom colliding with a grain will stick to it) is equal to 1 for all grain species. The onset of grain condensation is controlled by the temperature and density in the ejecta, whereas the grain composition depends on the chemical composition, which, in turn, depends on the nature of the SN progenitor (mass, metallicity, rotation, explosion energy). While the ejecta expands, we follow the formation and destruction rates of CO, SiO, C_2, O_2 molecules (which play an important role in subtracting gas-phase elements) and the condensation of seven different grain species: amorphous carbon (AC), iron (Fe), corundum (Al_2O_3), magnetite (Fe_3O_4), enstatite ($MgSiO_3$), forsterite (Mg_2SiO_4), and quarz (SiO_2). Following Marassi et al. (2015), we investigate dust formation in FE/CE SNe adopting the thermal, dynamical, and chemical evolution of the ejecta predicted by the output of 1D SN explosion simulations. The initial time for the calculation ($t_{\rm ini}$) is fixed by requiring that the gas temperature at the radius of the He core, $R_{\rm He_{core}}$ reaches a temperature of $T_0 =$

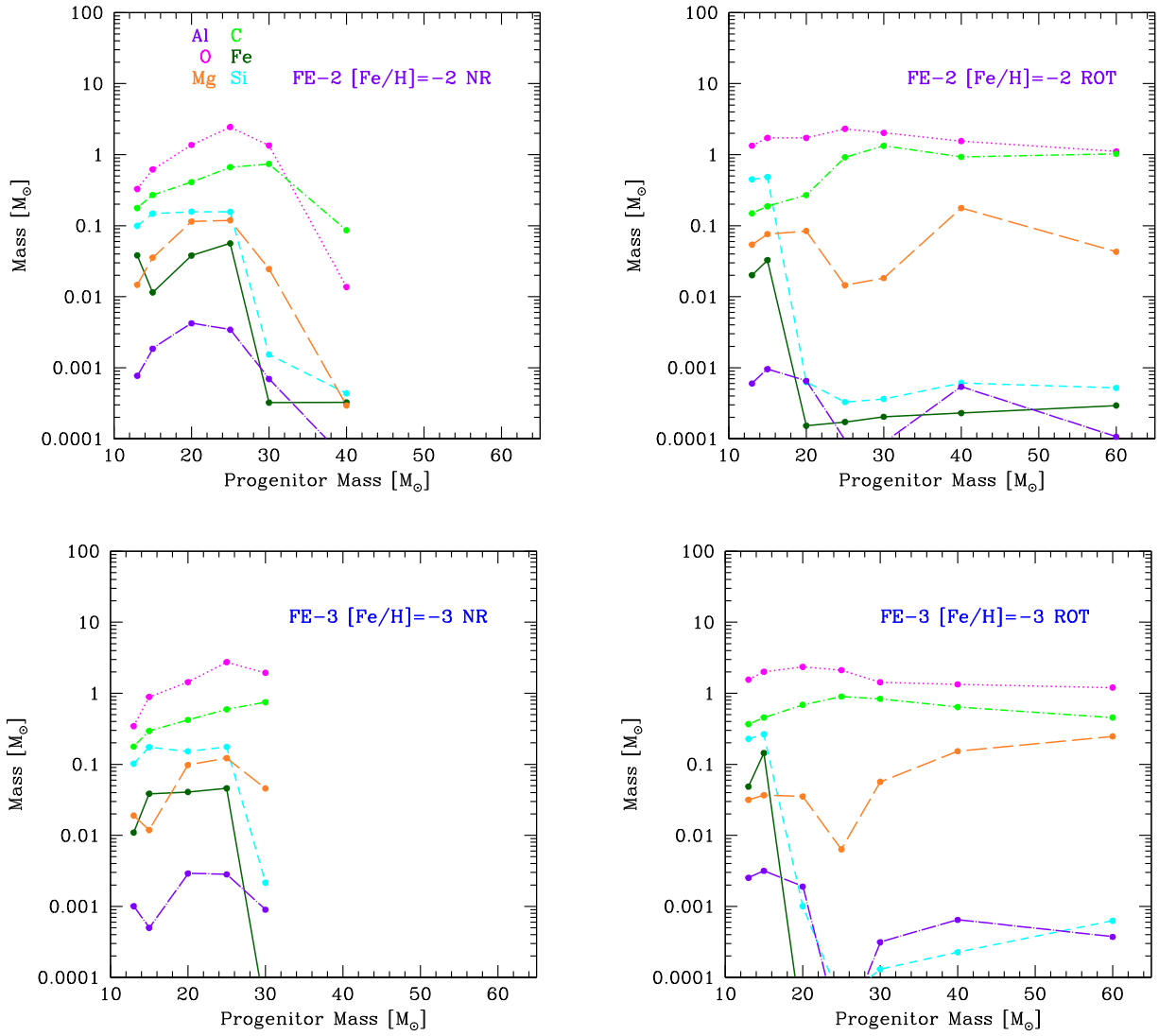

Figure 5. Initial C, O, Mg, Si, Al, and Fe elemental abundances in the ejecta (see the legenda) as a function of the progenitor mass for FE–SN models. Each pair of panels shows a different initial value of metallicity: set FE-2 (top left), set FE-3 (bottom left). In each pair, left-hand and right-hand panels show NR and ROT models.

10^4 K. At $t \geq t_{\rm ini}$, the ejecta follow an adiabatic expansion with a temperature evolution,

$$T = T_0 \left[1 + \frac{v_{\rm eje}}{R_0}(t - t_{\rm ini})\right]^{3(1-\gamma)}, \quad (1)$$

where $\gamma = 1.41$ is the adiabatic index, and T_0, R_0, and $v_{\rm eje}$ are the temperature and radius of the He core and ejecta velocity at $t = t_{\rm ini}$, respectively.

5 DUST GRID: DEPENDENCE ON FALLBACK, METALLICITY, AND ROTATION

In this section, we present the grid of SN dust yields for FE and CE SN models, discussing the effects of fallback, metallicity, and rotation.

We start by analysing the total mass of dust formed in FE-SN models as a function of metallicity and rotation. The progenitor mass, the SN type and the total mass of dust condensed in ROT and NR models are reported at fixed metallicity in Tables 9 and 10, respectively. The same data are also shown in Fig. 8.

For NR models, we find the total mass of dust to be in the range [0.16–1.2] $M_\odot$ for set FE0, [0.18–0.59] $M_\odot$ for set FE-1, [$1.3 \times 10^{-2} - 1.2$] $M_\odot$ for set FE-2, and [0.20–1.2] $M_\odot$ for set FE-3 (see Table 9). These results confirm previous theoretical predictions for type II-P SNe (Kozasa, Hasegawa & Nomoto 1989; Kozasa et al. 1991; Todini & Ferrara 2001; Nozawa et al. 2003; Bianchi & Schneider 2007; Cherchneff & Dwek 2010). We find that the effects of rotation depend on the mass and metallicity of the progenitor stars, as we discuss below. The resulting dust masses in ROT FE SN models are in the range [0.13–2.25] $M_\odot$ for set FE0, [$6.9 \times 10^{-2} - 0.65$] $M_\odot$ for set FE-1, [$2.6 \times 10^{-3} - 0.78$] $M_\odot$ for set FE-2, and [$6.3 \times 10^{-2} - 1.3$] $M_\odot$, for set FE-3 (see Table 10).

Fig. 8 shows that the dust mass does not monotonically increase with progenitor mass. Rather, it depends on the physical conditions of the ejecta, such as their temperature profile, their initial radius, and the gas-phase metal abundances that result from the formation and destruction of some key molecular species (Marassi et al. 2015). As shown in the left-hand panel of Fig. 8, for FE–NR models the dust mass increases with progenitor mass in the range [13–25] $M_\odot$ and then drops, due to fallback, particularly when [Fe/H] ≤ -2. The

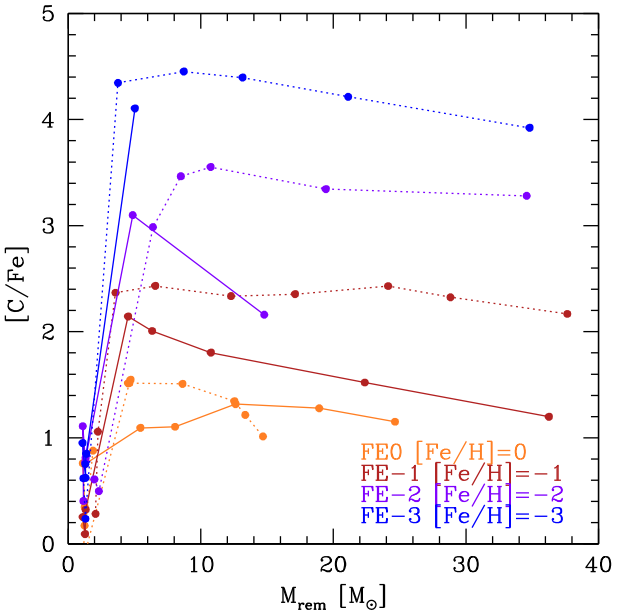

Figure 6. Initial [C/Fe] as a function of the remnant mass for NR (solid lines) and ROT (dotted lines) FE models with different initial metallicity (see the legenda).

increasing trend in the range [13–25] $M_\odot$ is mainly due to efficient destruction of molecules by Compton electrons coming from the ^{56}Ni decay in the ejecta, which favours dust condensation (Marassi et al. 2015).

In massive SN progenitors, the dust mass decreases due to the smaller amount of metals in the ejecta that survives the large fallback. In addition, the thermodynamical properties of the ejecta depend on the progenitor mass and, at the onset of adiabatic expansion, more massive SN have small initial radii, R_0 (see equation 1), and large ejecta density. The latter condition enables a more efficient formation of molecules, resulting in an efficient subtraction of gas-phase metals (Marassi et al. 2014, 2015).

In Fig. 9, we show the total dust depletion factor, f_{dep}, defined as the fraction of the initial ejecta metal mass (newly synthesized and pre-existing metals) that has condensed into dust, $f_{dep} = M_{dust}/M_{met}$, for FE NR (left-hand panel) and ROT (right-hand panel) models with different metallicity. For FE–NR SN models with mass in the range [13–25] $M_\odot$, f_{dep} varies between ∼0.3 and ∼0.6. For more massive SN models, the trend with progenitor mass changes depending on metallicity. The ejecta of FE0 and FE-1 models with $M > 40\,M_\odot$ have C > O and, despite the increase of fallback with progenitor mass, AC grains can form, leading to $f_{dep} \sim 0.7$ for both ROT and NR models. For most of the models in set FE-2 and FE-3, instead, C < O and the lower amount of metals in the ejecta leads to low values of f_{dep}.

The dependence of the dust composition on the progenitor mass and metallicity for NR FE models is presented in Fig. 10. This figure clearly shows that in models FE0 and FE-1 with progenitor masses $M < 30$–$40\,M_\odot$ a variety of grain species form, as a result of the large abundance of both pre-existing and newly synthesized metals in the ejecta. For larger progenitor masses, however, the most abundant dust species is AC. This is a consequence of the C > O composition and low abundances of heavier elements in the ejecta (see Fig. 4). Interestingly, in FE0 models with massive progenitors ($M \geq 60\,M_\odot$) ∼ (0.05–0.12) $M_\odot$ of iron grains form. The formation of solid iron is favoured by the efficient oxygen depletion on to CO molecules (which prevents the formation of Fe_3O_4 grains) and by the abundance of pre-existing iron in the ejecta. Finally, in set FE-2 and FE-3 silicates form only in the ejecta of [20–25] $M_\odot$ progenitors while in all the other models the dominant grain species are AC and Fe_3O_4.

In the right-hand panel of Fig. 8, we show the dust mass as a function of the progenitor mass for FE ROT SN models (see also Table 10). For all the metallicity data set, the most efficient dust factories are ROT models with masses in the range [13–15] $M_\odot$. This is not unexpected as metal abundances in the ejecta are larger than in NR models. In addition, in set FE0, FE-2, FE-3 these two progenitor masses have a non-zero ^{56}Ni mass in the ejecta (see Tables 1–4), which favours dust formation. For FE–ROT SN models with $20\,M_\odot < M < 40\,M_\odot$, the resulting dust mass decreases with progenitor mass. This is primarily due to different thermodynamical conditions in the ejecta, which enable more efficient molecule formation subtracting gas-phase metals. Also, the depletion factor is more scattered as it varies between $\sim 10^{-3}$ and 0.9. For $M \geq 40\,M_\odot$, the ejecta is mostly composed by carbon as a result of fallback, and the mass of dust is dominated by AC grains.

The dependence of the dust composition on progenitor mass and metallicity for ROT FE models is presented in Fig 11. The comparison with Fig. 10 allows to assess the impact of rotation. In general, ROT FE models are characterized by a dust composition that shows the same qualitative trends discussed for NR models: low progenitor masses are able to form a variety of dust species, while more massive progenitors mostly form AC grains. However, independent of metallicity, rotation leads to a more efficient formation of silicates and to a less efficient formation of AC grains in low-mass progenitors. Indeed, the physical conditions present in the ejecta of ROT models promote the formation of CO and SiO molecules that, in turn, affect the relative abundance of AC and silicates.

The dust mass produced by ROT and NR CE models are shown in Fig. 12 for different metallicity and progenitor masses. As expected, CE models lead to larger dust masses compared to FE models, and the dust mass increases with progenitor mass. In fact, the calibration of the explosion favours large ejecta and small remnant masses that, even for the more massive progenitors, never exceed ∼2 $M_\odot$ (see the lower panels in Fig. 3). In NR models (left-hand panels), the total dust mass is in the range [0.31–6.0] $M_\odot$ for set CE0, [0.30–6.2] $M_\odot$ for set CE-1, [0.35–5.0] $M_\odot$ for set CE-2, and [0.34–5.1] $M_\odot$ for set CE-3.

Rotation leads to more metal-rich ejecta, particularly by massive, low-metallicity progenitors (as a consequence of the more efficient rotation-induced mixing), and this increases the mass of dust formed. The opposite is true for solar metallicity massive progenitors, where a lower dust mass is produced in ROT models, because of the stronger mass-loss suffered during the pre-SN phase.

Overall, in ROT models we find that the total dust mass formed is in the range [0.65–3.8] $M_\odot$ for set CE0, [0.49–5.6] $M_\odot$ for set CE-1, [0.49–7.4] $M_\odot$ for set CE-2, and [0.72–6.6] $M_\odot$ for set CE-3.

For all CE models, we find that – independent of metallicity and rotation – the dust mass is dominated by silicates, as a consequence of the O > C composition and larger abundances of heavier elements in the ejecta, compared to FE models (see Fig. 7).

Finally, in Fig. 13 we show an example of how the grain size distribution is affected by different properties of the SN models. We fix the mass of the SN progenitor to be 20 $M_\odot$ and we consider a

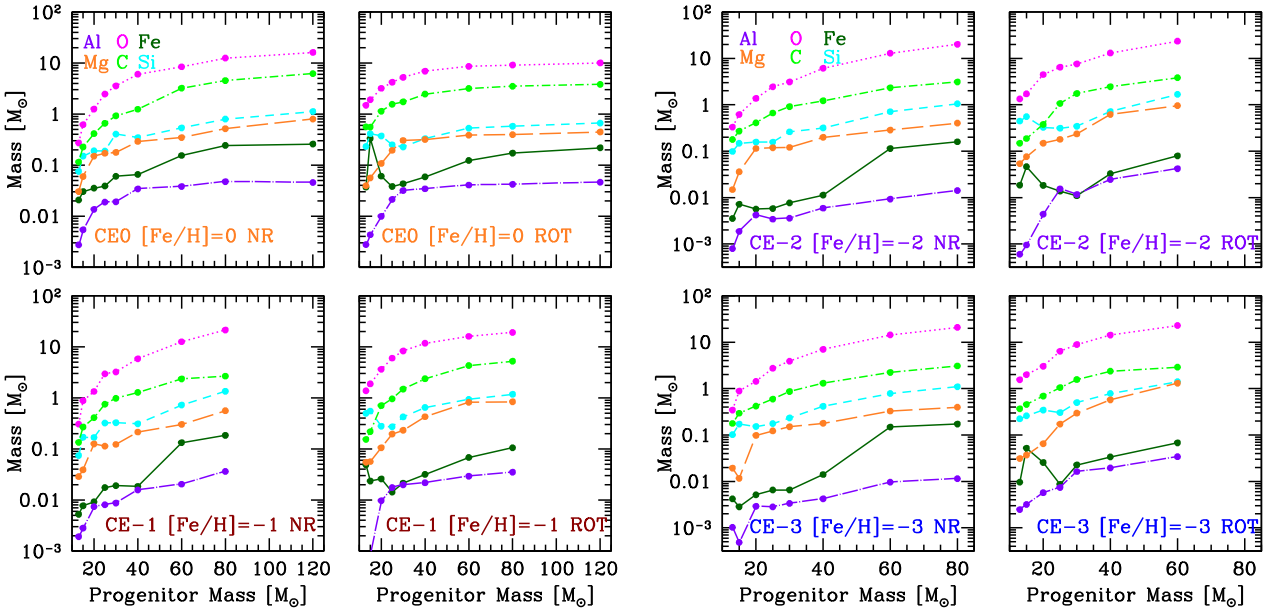

Figure 7. Initial C, O, Mg, Si, Al, and Fe elemental abundances in the ejecta (see the legenda) as a function of the progenitor mass for CE–SN models. Each pair of panels shows a different initial value of metallicity: set CE0 (top left), set CE-1 (bottom left), set CE-2 (top right), and set CE-3 (bottom right). In each pair, left-hand and right-hand panels show NR and ROT models.

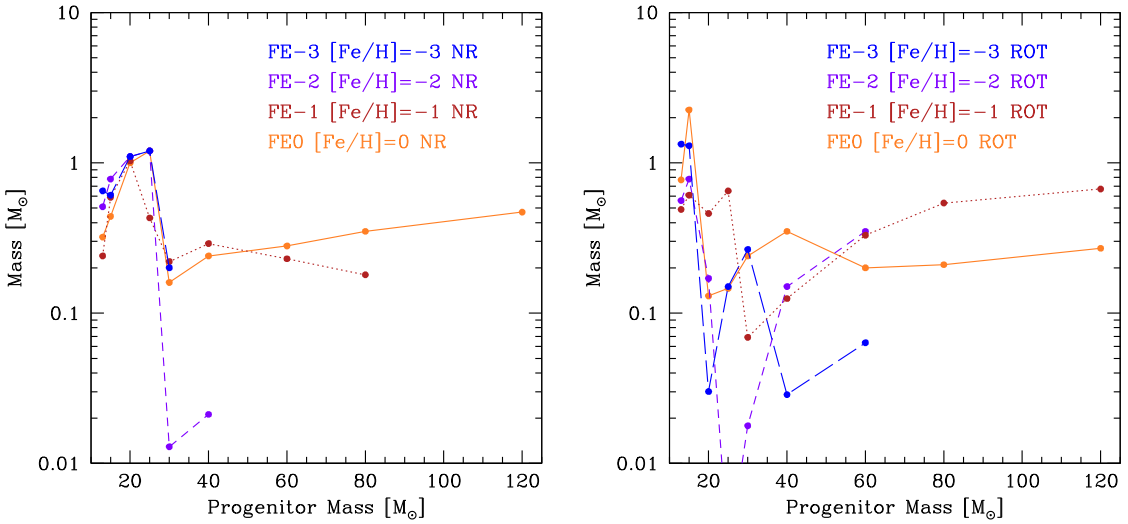

Figure 8. Mass of dust formed in the ejecta of FE SN models as a function of the mass of the progenitor star, for different values of metallicity. Left-hand and right-hand panels compare the results for NR and ROT models.

FE–NR model with [Fe/H] = 0 and [Fe/H] = −3 (leftmost panels) and a CE model with [Fe/H] = 0 and $v = 0, 300\,\mathrm{km\,s^{-1}}$ (rightmost panels).

The two SN models shown in the leftmost panels correspond to a type IIb SN at solar metallicity and to a type II-P SN at lower metallicity. The grain species that form are different and – for the type II-P – the grain sizes are shifted to lower values. This shift is mainly due to the different ejecta density when adiabatic expansion starts: the ejecta of the type II-P SN has an initial radius $R_0 \sim 1.5 \times 10^{15}$cm, whereas the type IIb ejecta has a smaller $R_0 \sim 3 \times 10^{14}$cm and, consequently, a greater ejecta density.

The FE–NR and CE–NR models shown in the first and third panels from the left have the same metallicity (FE0, CE0) and the same progenitor, He-core and remnant masses (see Tables 1 and 5), but a different amount of ^{56}Ni in the ejecta (0.33 $M_\odot$ for FE–NR and 5.8×10^{-2} $M_\odot$ for CE–NR), and slightly different initial conditions ($R_0 = 3.4 \times 10^{14}$cm for FE–NR and $R_0 = 2.9 \times 10^{14}$cm for FE–CE). The main difference is that the CE NR model has a lower dust mass due to inefficient destruction of molecules. In addition, the distribution of Fe_3O_4 grains is shifted towards lower radii, since ^{56}Ni decay does not provide enough iron to grow large Fe_3O_4 grains. Finally in the rightmost panels of Fig. 13, we compare the size distribution functions predicted for the CE0-NR model (a Type IIb SN) with the CE0-ROT model (a Type Ib SN): rotation causes the grain size distribution to shift towards lower radii, mainly due to the lower density in the ejecta.

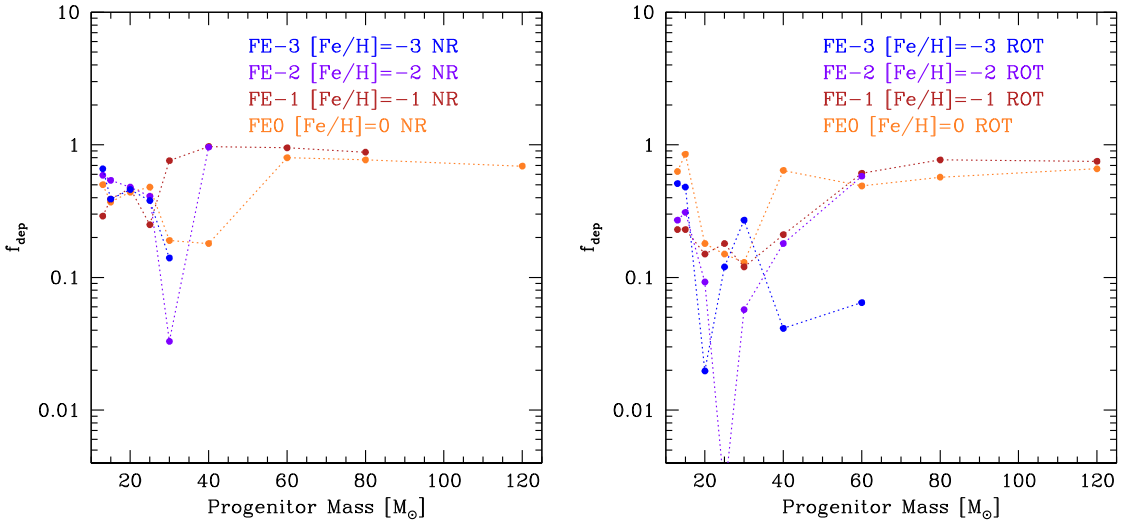

Figure 9. The dust depletion factor as a function of the initial progenitor mass, for FE NR (left-hand panel) and ROT (right-hand panel) models with different metallicity (see the legenda).

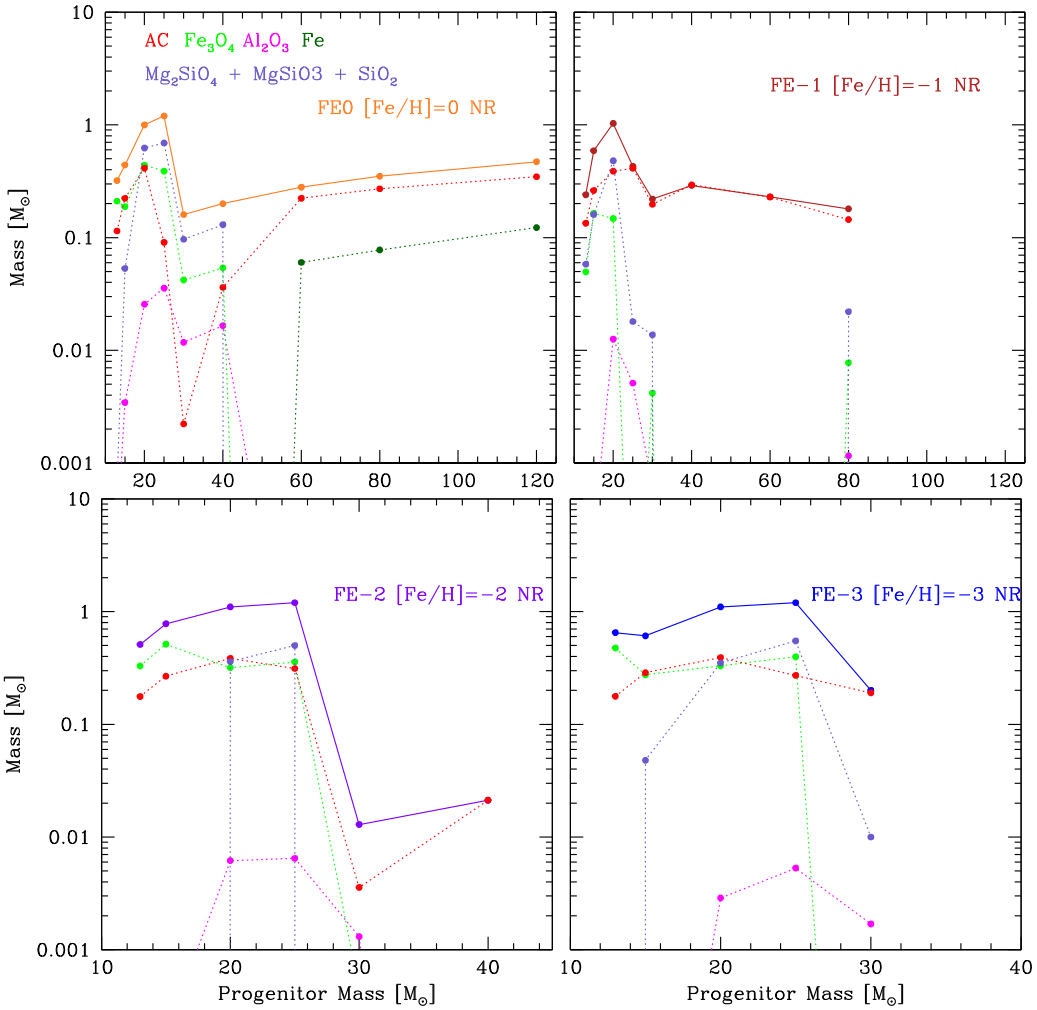

Figure 10. Mass of dust in different grain species for FE NR models as a function of the progenitor mass. Each panel corresponds to a different metallicity. In each panel, the upper solid line shows the total dust mass and the dotted lines represent the contribution of AC grains (red), Al_2O_3 (magenta), Fe_3O_4 (green), solid iron (dark green), and silicates and quarz, $MgSiO_3 + Mg_2SiO_4 + SiO_2$ (light blue, see the legenda).

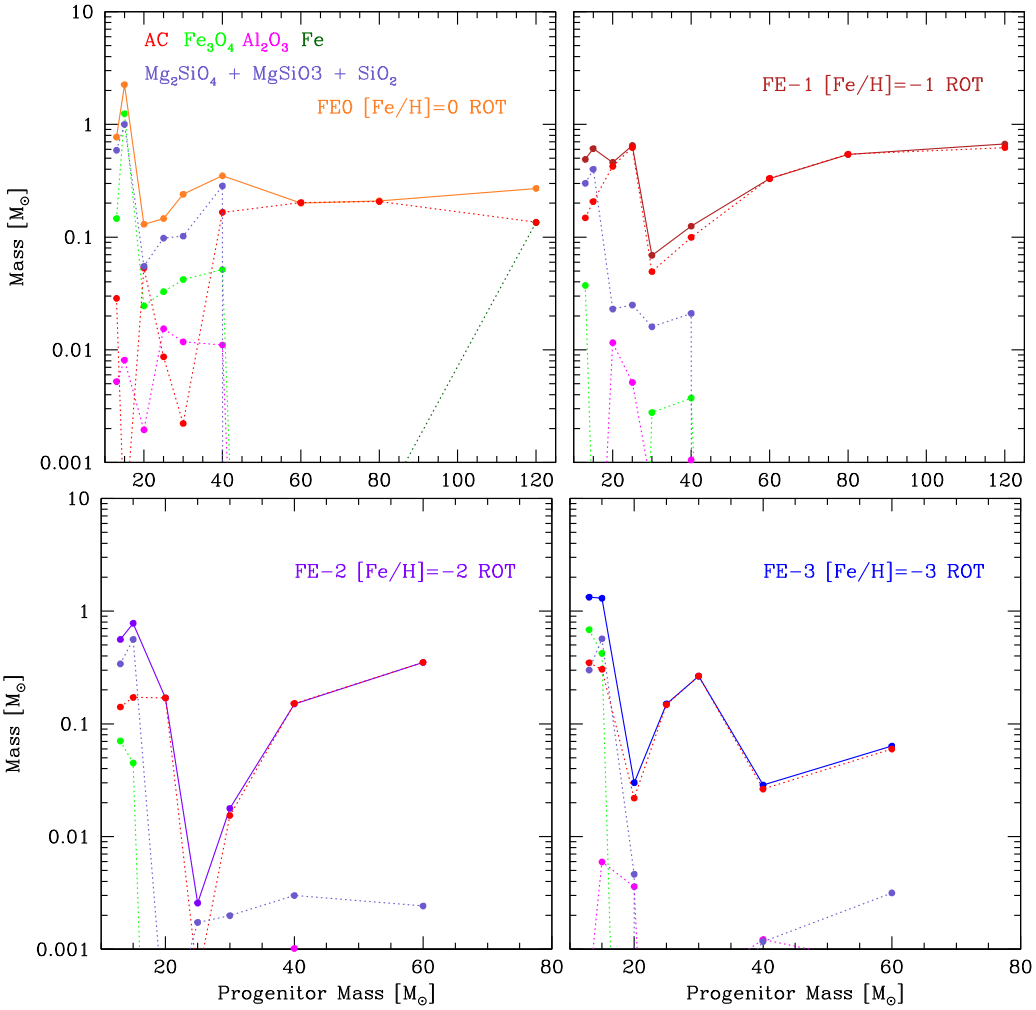

Figure 11. Mass of dust in different grain species for FE ROT models as a function of the progenitor mass. Each panel corresponds to a different metallicity. In each panel, the upper solid line shows the total dust mass and the dotted lines represent the contribution of AC grains (red), Al_2O_3 (magenta), Fe_3O_4 (green), solid iron (dark green), and silicates and quarz, $MgSiO_3 + Mg_2SiO_4 + SiO_2$ (light blue, see the legenda).

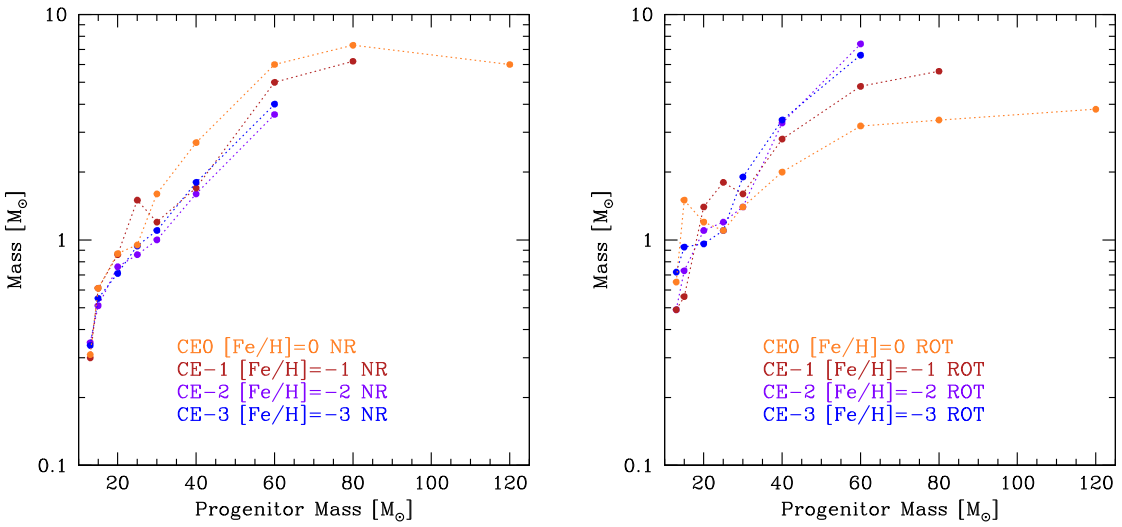

Figure 12. Mass of dust formed in the ejecta of CE SN models as a function of the mass of the progenitor star, for different values of metallicity. Left-hand and right-hand panels compare the results for NR and ROT models.

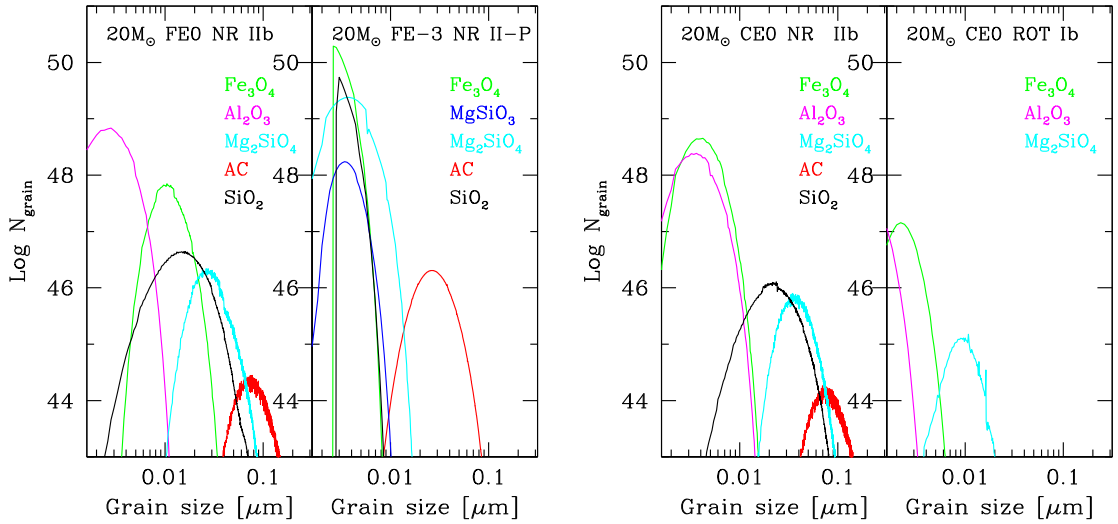

Figure 13. Grain size distribution function obtained for models with the same initial SN progenitor mass ($20\,M_\odot$), but different metallicity, rotation rates, and explosion energies (see the legenda). Colour coding of the different grain size distributions is the following: AC grains in red, Al_2O_3 in magenta, Fe_3O_4 in green, SiO_2 in black, $MgSiO_3$ in cyan, and Mg_2SiO_4 in blue.

6 CONCLUSIONS

We have analysed the dust mass produced in SN ejecta as a function of progenitor mass, rotation, metallicity, and fallback. The analysis of NR SN models that explode with a fixed energy of 1.2×10^{51} erg, shows that fallback has a large impact on both the composition and the mass of dust grains that form in the ejecta. Fallback has a major impact on the efficiency of dust formation in more massive SNe, particularly at low metallicity. As a result, SNe with progenitors $\lesssim$20–25 $M_\odot$ are generally more efficient at producing dust. They form between $\sim$0.1 and $\sim$1 $M_\odot$ of dust with a composition that is dominated by silicates, magnetite and carbon grains for progenitors at solar metallicity, and by magnetite and carbon grains at lower metallicity. SNe with more massive progenitors with [Fe/H] $= -1, -2, -3$ are able to form only carbon grains (with a contribution of iron grains from progenitors with [Fe/H] $= 0$). At lower metallicity fallback is too strong to allow significant dust production.

The above conclusions are only slightly modified by the adopted initial rotational velocity of the stars. When the same stars are assumed to be ROT with $v = 300\,km\,s^{-1}$, they reach the pre-supernova stage with larger cores and more metal-rich ejecta. This increases the efficiency of dust production, particularly for more massive progenitors. In addition, rotation favours more efficient silicate dust production by low-mass progenitors at all metallicity values, because these models have a higher abundance of Si and Mg in the ejecta.

Overall, the analysis of the SN sample with fixed explosion energy leads us to conclude that type Ib SNe are less dusty than type II-P and IIb, but this difference is due mainly to fallback and rotation.

It is interesting to note that massive stars that explode as SNe with a fixed explosion energy leaving massive remnants with masses $\gtrsim 5 M_\odot$ naturally lead to carbon enhanced ejecta with [C/Fe] >0.7, particularly if they are ROT. This agrees with previous studies that suggest that carbon enhanced metal poor stars have formed in the ashes of faint SNe or spinstars (Bonifacio et al. 2003; Limongi et al. 2003; Iwamoto et al. 2005; Meynet et al. 2006; Marassi et al. 2014; Maeder & Meynet 2015). Our findings indicate an increase in the carbon enhancement with decreasing metallicity whose implications will be investigated in the context of stellar archaeology in a future work.

The destructive effects of the reverse shock depend on the explosion energy, on the density of the circumstellar medium, on the clumpiness of the ejecta, and on the typical grain sizes and their distribution within the ejecta. A recent analysis of Bocchio et al. (2016) shows that models that are able to reproduce the dust mass inferred from observations of four nearby SN remnants predicts that only between 1 and 8 per cent of the currently observed mass will survive, resulting in an average SN effective dust yield of order $10^{-2}\,M_\odot$. Here we have focused on the first phase of dust production in SN ejecta and in the future we will address the impact of the reverse shock destruction. Based on our current findings, we expect a smaller dust survival fraction for grains formed in type Ib SNe, that are characterized by smaller sizes and hence are more easily destroyed.

Our findings are relevant to understand the role of SNe in dust enrichment at high redshifts and in the local Universe. Due to their short evolutionary time-scales, SNe can provide a fast and efficient dust formation channel at high redshift. The presence of dust grains in star-forming regions provide a fundamental formation pathway for the first low-mass and long-living stars (Schneider et al. 2003; Omukai et al. 2005; Schneider et al. 2012b,a; Chiaki et al. 2014, 2015; Marassi et al. 2014; de Bennassuti et al. 2015, 2017) and can help to understand the early dust enrichment of the interstellar medium of $z > 6$ quasar host galaxies (Valiante et al. 2009, 2011, 2014; Michałowski et al. 2010; Calura et al. 2014) and normal star-forming systems (Hirashita et al. 2014; Michałowski et al. 2015; Mancini et al. 2015, Graziani et al. in preparation).

Even in local galaxies, the short lifetimes of dust grains due to efficient destruction by interstellar shocks (Jones & Nuth 2011; Bocchio, Jones & Slavin 2014) require a fast replenishment by stars, aided by grain growth in dense interstellar gas when the metallicity is $Z \geq 0.1\,Z_\odot$ (Zhukovska, Gail & Trieloff 2008; Asano et al. 2013; Schneider et al. 2014; Schneider, Hunt & Valiante 2016; Zhukovska et al. 2016; Gioannini et al. 2017; Ginolfi et al. 2018). The starting point to understand the complex cycling of dust in the interstellar medium is dust production by SNe, and our study

aims to provide additional elements to assess how dust formation is affected by important physical properties of the progenitor stars and the explosions.

ACKNOWLEDGEMENTS

The research leading to these results has received funding from the European Research Council under the European Union's Seventh Framework Programme (FP/2007-2013) / ERC Grant Agreement no. 306476. AC and ML acknowledge financial support from the PRIN INAF (2014): Transient Universe: unveiling new types of stellar explosions with PESSTO (P.I. A. Pastorello). ML acknowledges the support by the ESO Visitor Program 2017-2018 and by the italian grants 'Premiale 2015 MITiC' (P.I. B. Garilli) and 'Premiale 2015 FIGARO' (P.I. G. Gemme).

REFERENCES

Asano R. S., Takeuchi T. T., Hirashita H., Nozawa T., 2013, MNRAS, 432, 637
Barlow M. J. et al., 2010, A&A, 518, L138
Beers T. C., Christlieb N., 2005, ARA&A, 43, 531
Bevan A., Barlow M. J., 2016, MNRAS, 456, 1269
Bevan A., Barlow M. J., Milisavljevic D., 2017, MNRAS, 465, 4044
Bianchi S., Schneider R., 2007, MNRAS, 378, 973
Biscaro C., Cherchneff I., 2014, A&A, 564, A25
Biscaro C., Cherchneff I., 2016, A&A, 589, A132
Bocchio M., Jones A. P., Slavin J. D., 2014, A&A, 570, A32
Bocchio M., Marassi S., Schneider R., Bianchi S., Limongi M., Chieffi A., 2016, A&A, 587, A157
Bonifacio P., Limongi M., Chieffi A., 2003, Nature, 422, 834
Calura F., Gilli R., Vignali C., Pozzi F., Pipino A., Matteucci F., 2014, MNRAS, 438, 2765
Cherchneff I., Dwek E., 2009, ApJ, 703, 642
Cherchneff I., Dwek E., 2010, ApJ, 713, 1
Chiaki G., Schneider R., Nozawa T., Omukai K., Limongi M., Yoshida N., Chieffi A., 2014, MNRAS, 439, 3121
Chiaki G., Marassi S., Nozawa T., Yoshida N., Schneider R., Omukai K., Limongi M., Chieffi A., 2015, MNRAS, 446, 2659
Chieffi A., Limongi M., 2003, PASA, 20, 324
Chieffi A., Limongi M., 2013, ApJ, 764, 21
Chieffi A., Limongi M., 2017, ApJ, 836, 79
Dayal P., Ferrara A., 2018, Phys. Rep., 780, 1
de Bennassuti M., Schneider R., Valiante R., Salvadori S., 2014, MNRAS, 445, 3039
de Bennassuti M., Schneider R., Valiante R., Salvadori S., 2015, MNRAS, 451, 2108
de Bennassuti M., Salvadori S., Schneider R., Valiante R., Omukai K., 2017, MNRAS, 465, 926
De Looze I., Barlow M. J., Swinyard B. M., Rho J., Gomez H. L., Matsuura M., Wesson R., 2017, MNRAS, 465, 3309
Dufton P. L. et al., 2006, A&A, 457, 265
Dunne L. et al., 2009, MNRAS, 394, 1307
Gall C., Hjorth J., Andersen A. C., 2011, A&A Rev., 19, 43
Ginolfi M., Graziani L., Schneider R., Marassi S., Valiante R., Dell'Agli F., Ventura P., Hunt L. K., 2018, MNRAS, 473, 4538
Gioannini L., Matteucci F., Vladilo G., Calura F., 2017, MNRAS, 464, 985
Gomez H. L. et al., 2012, ApJ, 760, 96
Hachinger S., Mazzali P. A., Taubenberger S., Hillebrandt W., Nomoto K., Sauer D. N., 2012, MNRAS, 422, 70
Hamuy M., 2003, ApJ, 582, 905
Heger A., Woosley S. E., 2002, ApJ, 567, 532
Hirashita H., Ferrara A., Dayal P., Ouchi M., 2014, MNRAS, 443, 1704
Hunter I., Lennon D. J., Dufton P. L., Trundle C., Simón-Díaz S., Smartt S. J., Ryans R. S. I., Evans C. J., 2008, A&A, 479, 541
Hunter D. J. et al., 2009, A&A, 508, 371
Indebetouw R. et al., 2014, ApJ, 782, L2
Iwamoto N., Umeda H., Tominaga N., Nomoto K., Maeda K., 2005, Science, 309, 451
Jones A. P., Nuth J. A., 2011, A&A, 530, A44
Kozasa T., Hasegawa H., Nomoto K., 1989, ApJ, 344, 325
Kozasa T., Hasegawa H., Nomoto K., 1991, A&A, 249, 474
Kozasa T., Nozawa T., Tominaga N., Umeda H., Maeda K., Nomoto K., 2009, in Henning T., Grün E., Steinacker J., eds, ASP Conf. Ser. Vol. 414, Cosmic Dust – Near and Far, Astron. Soc. Pac., San Francisco. p. 43
Lazzati D., Heger A., 2016, ApJ, 817, 134
Limongi M., 2017, Supernovae from Massive Stars, Springer International Publishing, Cham, 1
Limongi M., Chieffi A., 2012, ApJS, 199, 38
Limongi M., Chieffi A., 2018, ApJS, 237, 13
Limongi M., Chieffi A., Bonifacio P., 2003, ApJ, 594, L123
Maeder A., Meynet G., 2015, A&A, 580, A32
Mancini M., Schneider R., Graziani L., Valiante R., Dayal P., Maio U., Ciardi B., Hunt L. K., 2015, MNRAS, 451, L70
Marassi S., Chiaki G., Schneider R., Limongi M., Omukai K., Nozawa T., Chieffi A., Yoshida N., 2014, ApJ, 794, 100
Marassi S., Schneider R., Limongi M., Chieffi A., Bocchio M., Bianchi S., 2015, MNRAS, 454, 4
Matsuura M. et al., 2011, Science, 333, 1258
Matsuura M. et al., 2015, ApJ, 800, 50
Meynet G., Ekström S., Maeder A., 2006, A&A, 447, 623
Micelotta E. R., Dwek E., Slavin J. D., 2016, A&A, 590, A65
Michałowski M. J. et al., 2015, A&A, 582, A78
Michałowski M. J., Murphy E. J., Hjorth J., Watson D., Gall C., Dunlop J. S., 2010, A&A, 522, A15
Nomoto K., Kobayashi C., Tominaga N., 2013, ARA&A, 51, 457
Nozawa T., Kozasa T., 2013, ApJ, 776, 24
Nozawa T., Kozasa T., Umeda H., Maeda K., Nomoto K., 2003, ApJ, 598, 785
Nozawa T., Kozasa T., Habe A., Dwek E., Umeda H., Tominaga N., Maeda K., Nomoto K., 2007, ApJ, 666, 955
Nozawa T., Kozasa T., Tominaga N., Maeda K., Umeda H., Nomoto K., Krause O., 2010, ApJ, 713, 356
Nozawa T., Maeda K., Kozasa T., Tanaka M., Nomoto K., Umeda H., 2011, ApJ, 736, 45
Nozawa T., Wakita S., Hasegawa Y., Kozasa T., 2015, ApJ, 811, L39
Omukai K., Tsuribe T., Schneider R., Ferrara A., 2005, ApJ, 626, 627
Otsuka M. et al., 2010, A&A, 518, L139
Ramírez-Agudelo O. H. et al., 2017, A&A, 600, A81
Rho J., Gomez H. L., Boogert A., Smith M. W. L., Lagage P.-O., Dowell D., Clark C. J. R., 2017, MNRAS, 479, 5101
Sarangi A., Cherchneff I., 2013, ApJ, 776, 107
Sarangi A., Cherchneff I., 2015, A&A, 575, A95
Schneider R., Ferrara A., Salvaterra R., Omukai K., Bromm V., 2003, Nature, 422, 869
Schneider R., Ferrara A., Salvaterra R., 2004, MNRAS, 351, 1379
Schneider R., Omukai K., Bianchi S., Valiante R., 2012a, MNRAS, 419, 1566
Schneider R., Omukai K., Limongi M., Ferrara A., Salvaterra R., Chieffi A., Bianchi S., 2012b, MNRAS, 423, L60
Schneider R., Valiante R., Ventura P., dell'Agli F., Di Criscienzo M., Hirashita H., Kemper F., 2014, MNRAS, 442, 1440
Schneider R., Hunt L., Valiante R., 2016, MNRAS, 457, 1842
Silvia D. W., Smith B. D., Shull J. M., 2010, ApJ, 715, 1575
Silvia D. W., Smith B. D., Shull J. M., 2012, ApJ, 748, 12
Sluder A., Milosavljević M., Montgomery M. H., 2018, MNRAS, 480, 5580
Smartt S. J., 2009, ARA&A, 47, 63
Temim T., Dwek E., Tchernyshyov K., Boyer M. L., Meixner M., Gall C., Roman-Duval J., 2015, ApJ, 799, 158
Temim T., Dwek E., Arendt R. G., Borkowski K. J., Reynolds S. P., Slane P., Gelfand J. D., Raymond J. C., 2017, ApJ, 836, 129
Todini P., Ferrara A., 2001, MNRAS, 325, 726
Umeda H., Nomoto K., 2002, ApJ, 565, 385

Valiante R., Schneider R., Bianchi S., Andersen A. C., 2009, MNRAS, 397, 1661
Valiante R., Schneider R., Salvadori S., Bianchi S., 2011, MNRAS, 416, 1916
Valiante R., Schneider R., Salvadori S., Gallerani S., 2014, MNRAS, 444, 2442
Woosley S. E., Weaver T. A., 1995, NASA STI/Recon Technical Report N, 96
Zhukovska S., Gail H.-P., Trieloff M., 2008, A&A, 479, 453
Zhukovska S., Dobbs C., Jenkins E. B., Klessen R. S., 2016, ApJ, 831, 147

APPENDIX

In this appendix, we report all the Tables. In particular, Tables 9–12 show – for NR and ROT FE and CE models – the progenitor mass, M ($M_\odot$), SN type, and the total mass of dust for each metallicity data set; in Tables 1–8, we report the physical properties of FE and CE NR and ROT SN models: the progenitor mass M ($M_\odot$), $M_{\rm preSN}$ ($M_\odot$) (mass of the star at the time of explosion), SN type, $M_{\rm rem}$ ($M_\odot$), $M_{\rm He_{core}}$($M_\odot$), $M_{\rm eje}$ ($M_\odot$), and ^{56}Ni ($M_\odot$).

Table 1. Properties of the NR and ROT fixed-energy models, FE with [Fe/H] = 0 (FE0): progenitor mass (M), pre-SN mass ($M_{\rm preSN}$), SN-type, explosion energy ($E_{\rm exp}$), remnant-mass ($M_{\rm rem}$), helium core mass ($M_{\rm He_{core}}$), ejecta mass ($M_{\rm eje}$), and the nichel 56 mass (^{56}Ni).

M ($M_\odot$)	$M_{\rm preSN}$ ($M_\odot$)	SN-type	$E_{\rm exp}$	$M_{\rm rem}$ ($M_\odot$)	$M_{\rm He_{core}}$ ($M_\odot$)	$M_{\rm eje}$ ($M_\odot$)	M (^{56}Ni) ($M_\odot$)
				FE0 NR			
13	11.86	II-P	1.2	1.24	4.0	10.62	0.15
15	13.23	II-P	1.2	1.25	4.88	11.98	0.14
20	7.54	IIb	1.2	1.09	7.18	6.45	0.33
25	8.54	IIb	1.2	1.27	8.54	7.27	0.24
30	10.83	Ib	1.2	5.45	10.83	5.38	0.00
40	14.14	Ib	1.2	8.06	14.14	6.08	0.00
60	16.95	Ib	1.2	12.62	16.95	4.33	0.00
80	22.71	Ib	1.2	18.93	22.72	3.78	0.00
120	27.87	Ib	1.2	24.64	27.87	3.23	0.00
				FE0 ROT			
13	5.35	Ib	1.2	1.87	5.35	3.48	0.072
15	6.22	Ib	1.2	1.01	6.22	5.21	0.41
20	8.18	Ib	1.2	4.61	8.18	3.57	0.00
25	9.48	Ib	1.2	4.70	9.48	4.78	0.00
30	11.20	Ib	1.2	4.52	11.20	6.68	0.00
40	13.81	Ib	1.2	8.62	13.81	5.19	0.00
60	16.64	Ib	1.2	12.53	16.64	4.11	0.00
80	17.48	Ib	1.2	13.35	17.48	4.13	0.00
120	18.59	Ib	1.2	14.69	18.58	3.9	0.00

Table 2. Properties of the NR and ROT fixed-energy models, FE with [Fe/H] = −1 (FE-1): progenitor mass (M), pre-SN mass ($M_{\rm preSN}$), SN-type, explosion energy ($E_{\rm exp}$), remnant-mass ($M_{\rm rem}$), helium core mass ($M_{\rm He_{core}}$), ejecta mass ($M_{\rm eje}$), and the nichel 56 mass (^{56}Ni).

M ($M_\odot$)	$M_{\rm preSN}$ ($M_\odot$)	SN-type	$E_{\rm exp}$	$M_{\rm rem}$ ($M_\odot$)	$M_{\rm He_{core}}$($M_\odot$)	$M_{\rm eje}$ ($M_\odot$)	M (^{56}Ni) ($M_\odot$)
				FE-1 NR			
13	12.48	II-P	1.2	1.10	4.19	11.38	0.00
15	14.17	II-P	1.2	1.27	5.14	12.9	0.00
20	18.35	II-P	1.2	1.32	7.41	17.03	0.00
25	20.57	II-P	1.2	4.52	10.02	16.5	0.00
30	28.27	II-P	1.2	6.33	11.72	21.94	0.00
40	28.71	II-P	1.2	10.76	16.42	17.95	0.00
60	41.96	II-P	1.2	22.37	26.52	19.59	0.00
80	39.85	Ib	1.2	36.25	38.86	3.6	0.00
				FE-1 ROT			
13	10.67	II-P	1.2	2.07	5.46	8.6	0.00
15	11.14	II-P	1.2	2.24	5.92	9.0	0.00
20	17.09	II-P	1.2	3.57	7.47	13.52	0.00
25	18.38	II-P	1.2	6.57	11.63	11.81	0.00
30	15.95	Ib	1.2	12.28	15.95	3.67	0.00
40	20.68	Ib	1.2	17.11	20.68	3.57	0.00
60	27.53	Ib	1.2	24.13	27.53	3.4	0.00
80	32.07	Ib	1.2	28.83	32.07	3.24	0.00
120	40.49	Ib	1.2	37.64	40.49	2.85	0.00

Table 3. Properties of the NR and ROT fixed-energy models, FE with [Fe/H] $= -2$ (FE-2): progenitor mass (M), pre-SN mass ($M_{\rm preSN}$), SN-type, explosion energy ($E_{\rm exp}$), remnant-mass ($M_{\rm rem}$), helium core mass ($M_{\rm He_{core}}$), ejecta mass ($M_{\rm eje}$), and the nichel 56 mass (^{56}Ni). For failed SN models, we only show the pre-SN and final remnant masses.

M ($M_\odot$)	$M_{\rm preSN}$ ($M_\odot$)	SN-type	$E_{\rm exp}$	$M_{\rm rem}$ ($M_\odot$)	$M_{\rm He_{core}}$($M_\odot$)	$M_{\rm eje}$ ($M_\odot$)	M (^{56}Ni) ($M_\odot$)
				FE-2 NR			
13	12.96	II-P	1.2	1.15	4.25	11.81	0.24
15	14.78	II-P	1.2	1.10	5.07	13.68	0.37
20	19.72	II-P	1.2	1.28	7.34	18.44	0.23
25	24.65	II-P	1.2	1.33	9.67	23.32	0.26
30	29.86	II-P	1.2	4.86	11.37	25	0.00
40	39.74	II-P	1.2	14.78	16.38	24.96	0.00
60	59.61	failed SN	1.2	28.87	–	–	–
80	78.59	failed SN	1.2	42.34	–	–	–
				FE-2 ROT			
13	11.44	II-P	1.2	1.97	5.43	9.47	0.051
15	13.67	II-P	1.2	2.31	5.86	11.36	0.00
20	16.79	II-P	1.2	6.39	9.79	10.4	0.00
25	13.16	Ib	1.2	8.49	13.16	4.67	0.00
30	15.06	Ib	1.2	10.74	15.06	4.32	0.00
40	22.94	Ib	1.2	19.43	22.94	3.51	0.00
60	37.41	Ib	1.2	34.57	37.41	2.84	0.00

Table 4. Properties of the NR and ROT fixed-energy models, FE with [Fe/H] $= -3$ (FE-3): progenitor mass (M), pre-SN mass ($M_{\rm preSN}$), SN-type, explosion energy ($E_{\rm exp}$), remnant-mass ($M_{\rm rem}$), helium core mass ($M_{\rm He_{core}}$), ejecta mass ($M_{\rm eje}$), and the nichel 56 mass (^{56}Ni). For failed SN models, we only show the pre-SN and final remnant masses.

M ($M_\odot$)	$M_{\rm preSN}$ ($M_\odot$)	SN-type	$E_{\rm exp}$	$M_{\rm rem}$ ($M_\odot$)	$M_{\rm He_{core}}$[$M_\odot$]	$M_{\rm eje}$ ($M_\odot$)	M (^{56}Ni) ($M_\odot$)
				FE-3 NR			
13	12.97	II-P	1.2	1.09	4.10	11.88	0.34
15	14.95	II-P	1.2	1.31	5.07	13.64	0.20
20	19.79	II-P	1.2	1.29	7.14	18.5	0.24
25	24.63	II-P	1.2	1.37	9.55	23.26	0.28
30	29.97	II-P	1.2	5.04	12	24.93	0.00
40	39.96	Failed SN	1.2	17.55	–	–	–
60	59.94	Failed SN	1.2	31.12	–	–	–
80	79.90	Failed SN	1.2	45.62	–	–	–
				FE-3 ROT			
13	12.77	II-P	1.2	1.14	4.87	11.63	0.49
15	13.78	II-P	1.2	1.30	6.06	13.7	0.30
20	19.96	II-P	1.2	3.75	7.85	16.21	0.00
25	13.29	Ib	1.2	8.71	12.91	4.58	0.00
30	17.06	Ib	1.2	13.15	16.80	3.91	0.00
40	24.48	Ib	1.2	21.12	24.48	3.36	0.00
60	38.14	Ib	1.2	34.79	38.14	3.35	0.00

Table 5. Properties of the NR and ROT calibrated-energy models, CE with [Fe/H] = 0 (CE0): progenitor mass (M), pre-SN mass ($M_{\rm preSN}$), SN-type, explosion energy ($E_{\rm exp}$), remnant-mass ($M_{\rm rem}$), helium core mass ($M_{\rm He_{core}}$), ejecta mass ($M_{\rm eje}$), and the nichel 56 mass (^{56}Ni).

M ($M_\odot$)	$M_{\rm preSN}$ ($M_\odot$)	SN-type	$E_{\rm exp}$	$M_{\rm rem}$ ($M_\odot$)	$M_{\rm He_{core}}$($M_\odot$)	$M_{\rm eje}$ ($M_\odot$)	M (^{56}Ni) ($M_\odot$)
				CE0 NR			
13	11.86	II-P	0.56	1.50	4.00	10.36	0.015
15	13.23	II-P	0.73	1.54	4.88	11.69	0.024
20	7.54	IIb	0.67	1.47	7.18	6.07	0.058
25	8.54	IIb	0.94	1.54	8.54	7.0	0.11
30	10.83	Ib	1.71	1.92	10.83	8.91	0.19
40	14.14	Ib	1.92	1.64	14.14	12.5	0.46
60	16.95	Ib	2.59	1.37	16.95	15.58	0.62
80	22.71	Ib	3.49	1.35	22.71	21.36	0.77
120	27.87	Ib	5.94	1.51	27.87	26.36	0.97
				CE0 ROT			
13	5.35	Ib	1.23	1.97	5.35	3.38	0.015
15	6.22	Ib	0.93	1.99	6.22	4.23	0.024
20	8.18	Ib	2.03	2.27	8.18	5.91	0.058
25	9.48	Ib	1.77	1.97	9.48	7.51	0.11
30	11.20	Ib	1.78	1.80	11.20	9.4	0.19
40	13.81	Ib	2.49	1.83	13.81	11.98	0.46
60	16.64	Ib	2.76	1.45	16.64	15.19	0.63
80	17.48	Ib	2.83	1.42	17.48	16.06	0.64
120	18.59	Ib	3.01	1.44	18.59	17.15	0.68

Table 6. Properties of the NR and ROT calibrated-energy models, CE with [Fe/H] = −1 (CE-1): progenitor mass (M), pre-SN mass ($M_{\rm preSN}$), SN-type, explosion energy ($E_{\rm exp}$), remnant-mass ($M_{\rm rem}$), helium core mass ($M_{\rm He_{core}}$), ejecta mass ($M_{\rm eje}$), and the nichel 56 mass (^{56}Ni).

M ($M_\odot$)	$M_{\rm preSN}$ ($M_\odot$)	SN-type	$E_{\rm exp}$	$M_{\rm rem}$ ($M_\odot$)	$M_{\rm He_{core}}$($M_\odot$)	$M_{\rm eje}$ ($M_\odot$)	M (^{56}Ni) ($M_\odot$)
				CE-1 NR			
13	12.48	II-P	0.50	1.52	4.19	10.96	0.015
15	14.17	II-P	0.82	1.60	5.14	12.57	0.024
20	18.35	II-P	0.88	1.61	7.41	16.74	0.058
25	20.57	II-P	1.49	1.97	10.00	18.06	0.11
30	28.27	II-P	1.58	1.88	11.72	26.39	0.19
40	28.71	II-P	1.87	1.64	16.46	27.07	0.46
60	41.96	II-P	3.56	1.39	26.58	40.57	0.85
80	39.85	Ib	5.68	1.46	38.86	38.39	1.23
				CE-1 ROT			
13	10.67	II-P	1.30	2.07	5.46	8.6	0.015
15	11.14	II-P	1.44	2.10	6.02	9.04	0.024
20	17.09	II-P	1.92	2.21	7.54	14.88	0.058
25	18.38	II-P	2.22	2.24	11.83	16.14	0.11
30	15.95	Ib	3.08	2.50	15.95	13.45	0.19
40	20.68	Ib	3.93	2.36	20.68	18.32	0.46
60	27.53	Ib	5.11	2.01	27.53	25.52	0.76
80	32.07	Ib	5.90	1.88	32.07	30.19	0.79

Table 7. Properties of the NR and ROT calibrated-energy models, CE with [Fe/H] $= -2$ (CE-2): progenitor mass (M), pre-SN mass ($M_{\rm preSN}$), SN-type, explosion energy ($E_{\rm exp}$), remnant-mass ($M_{\rm rem}$), helium core mass ($M_{\rm He_{core}}$), ejecta mass ($M_{\rm eje}$), and the nichel 56 mass (^{56}Ni).

M ($M_\odot$)	$M_{\rm preSN}$ ($M_\odot$)	SN-type	$E_{\rm exp}$	$M_{\rm rem}$ ($M_\odot$)	$M_{\rm He_{core}}$($M_\odot$)	$M_{\rm eje}$ ($M_\odot$)	M (^{56}Ni) ($M_\odot$)
				CE-2 NR			
13	12.96	II-P	0.64	1.58	4.24	11.38	0.015
15	14.78	II-P	0.64	1.54	5.10	13.24	0.024
20	19.72	II-P	0.88	1.63	7.34	18.09	0.058
25	24.65	II-P	1.04	1.71	9.67	22.94	0.11
30	29.86	II-P	1.30	1.74	11.37	28.12	0.19
40	39.74	II-P	1.92	1.69	16.38	38.05	0.46
60	59.61	II-P	3.68	1.43	26.85	58.18	0.88
80	78.59	II-P	5.35	1.43	37.84	77.16	1.15
				CE-2 ROT			
13	11.44	II-P	1.23	2.02	5.43	9.42	0.015
15	13.67	II-P	1.51	2.15	5.86	11.52	0.024
20	11.44	II-P	2.38	2.65	9.79	8.79	0.058
25	13.16	Ib	2.51	2.37	13.00	10.79	0.11
30	15.06	Ib	2.70	2.33	15.06	12.73	0.19
40	22.94	Ib	4.26	2.44	22.94	20.5	0.46
60	37.41	Ib	4.83	1.95	37.41	35.46	1.49

Table 8. Properties of the NR and ROT calibrated-energy models, CE with [Fe/H] $= -3$ (CE-3): progenitor mass (M), pre-SN mass ($M_{\rm preSN}$), SN-type, explosion energy ($E_{\rm exp}$), remnant-mass ($M_{\rm rem}$), helium core mass ($M_{\rm He_{core}}$), ejecta mass ($M_{\rm eje}$), and the nichel 56 mass (^{56}Ni).

M ($M_\odot$)	$M_{\rm preSN}$ ($M_\odot$)	SN-type	$E_{\rm exp}$	$M_{\rm rem}$ ($M_\odot$)	$M_{\rm He_{core}}$($M_\odot$)	$M_{\rm eje}$ ($M_\odot$)	M (^{56}Ni) ($M_\odot$)
				CE-3 NR			
13	12.97	II-P	0.54	1.55	4.12	11.42	0.015
15	14.95	II-P	0.88	1.68	5.07	13.27	0.024
20	19.79	II-P	0.89	1.65	7.18	18.14	0.058
25	24.63	II-P	1.14	1.75	9.55	22.88	0.11
30	29.97	II-P	1.38	1.72	11.99	28.25	0.19
40	39.96	II-P	2.26	1.74	16.98	38.22	0.46
60	59.94	II-P	4.03	1.39	27.01	58.55	0.95
80	79.90	II-P	5.68	1.44	37.93	78.46	1.16
				CE-3 ROT			
13	12.77	II-P	0.78	1.80	4.57	10.97	0.015
15	13.78	II-P	1.10	2.09	5.52	11.69	0.024
20	19.96	II-P	1.86	2.18	7.85	17.78	0.058
25	13.29	Ib	2.52	2.38	12.79	10.91	0.11
30	17.06	Ib	2.93	2.34	16.78	14.72	0.19
40	24.48	Ib	4.59	2.52	24.48	21.96	0.46
60	38.14	Ib	7.07	2.13	38.14	36.01	0.96

Table 9. Dust masses produced by the NR fixed-energy models (FE) of different metallicity: FE0 ([Fe/H] $= 0$), FE-1 ([Fe/H] $= -1$), FE-2 ([Fe/H] $= -2$), FE-3 ([Fe/H] $= -3$). Progenitor mass (M), SN type, and dust mass ($M_{\rm dust}$). We also indicate the failed SN or pair unstable models for which dust formation has not been computed.

					FE NR			
	FE0		FE-1		FE-2		FE-3	
M ($M_\odot$)	SN-type	$M_{\rm dust}$ ($M_\odot$)	SN-type	$M_{\rm dust}$ ($M_\odot$)	SN-type	$M_{\rm dust}$ ($M_\odot$)	SN-type	$M_{\rm dust}$ ($M_\odot$)
13	II-P	0.32	II-P	0.24	II-P	0.51	II-P	0.65
15	II-P	0.44	II-P	0.59	II-P	0.78	II-P	0.61
20	IIb	1.0	II-P	1.03	II-P	1.1	II-P	1.1
25	IIb	1.2	II-P	0.43	II-P	1.2	II-P	1.2
30	Ib	0.16	II-P	0.22	II-P	1.3×10^{-2}	II-P	0.20
40	Ib	0.24	II-P	0.29	II-P	2.1×10^{-2}	Failed SN	–
60	Ib	0.28	II-P	0.23	Failed SN	–	Failed SN	–
80	Ib	0.35	Ib	0.18	Failed SN	–	Failed SN	–
120	Ib	0.47	Pair-unstable	–	Pair-unstable	–	Pair-unstable	–

Table 10. Dust masses produced by the ROT fixed-energy models (FE) of different metallicity: FE0 ([Fe/H] = 0), FE-1 ([Fe/H] = −1), FE-2 ([Fe/H] = −2), FE-3 ([Fe/H] = −3). Progenitor mass (M), SN type, and dust mass ($M_{\rm dust}$). We also indicate the pair unstable models for which dust formation has not been computed.

	FE ROT							
	FE0		FE-1		FE-2		FE-3	
M ($M_\odot$)	SN-type	$M_{\rm dust}$ ($M_\odot$)	SN-type	$M_{\rm dust}$ ($M_\odot$)	SN-type	$M_{\rm dust}$ ($M_\odot$)	SN-type	$M_{\rm dust}$ ($M_\odot$)
13	Ib	0.77	II-P	0.49	II-P	0.56	II-P	1.3
15	Ib	2.25	II-P	0.61	II-P	0.78	II-P	1.3
20	Ib	0.13	II-P	0.46	II-P	0.17	II-P	3.0×10^{-2}
25	Ib	0.15	II-P	0.65	Ib	2.6×10^{-3}	Ib	0.15
30	Ib	0.24	Ib	6.9×10^{-2}	Ib	1.8×10^{-2}	Ib	0.27
40	Ib	0.35	Ib	0.12	Ib	0.15	Ib	2.9×10^{-2}
60	Ib	0.20	Ib	0.33	Ib	0.35	Ib	6.3×10^{-2}
80	Ib	0.21	Ib	0.54	Pair-unstable	–	Pair-unstable	–
120	Ib	0.27	Ib	0.62	Pair-unstable	–	Pair-unstable	–

Table 11. Dust masses produced by NR calibrated-energy models (CE) of different metallicity: CE0 ([Fe/H] = 0), CE-1 ([Fe/H] = −1), CE-2 ([Fe/H] = −2), CE-3 ([Fe/H] = −3). Progenitor mass (M), SN type, and dust mass ($M_{\rm dust}$). We also indicate the pair unstable models for which dust formation has not been computed.

	CE NR							
	CE0		CE-1		CE-2		CE-3	
M ($M_\odot$)	SN-type	$M_{\rm dust}$ ($M_\odot$)	SN-type	$M_{\rm dust}$ ($M_\odot$)	SN-type	$M_{\rm dust}$ ($M_\odot$)	SN-type	$M_{\rm dust}$ ($M_\odot$)
13	II-P	0.31	II-P	0.30	II-P	0.35	II-P	0.34
15	II-P	0.61	II-P	0.61	II-P	0.51	II-P	0.55
20	IIb	0.87	II-P	0.86	II-P	0.76	II-P	0.71
25	IIb	0.95	II-P	1.50	Ib	0.86	Ib	0.94
30	Ib	1.6	Ib	1.2	Ib	1.0	Ib	1.1
40	Ib	2.7	Ib	1.7	Ib	1.6	Ib	1.8
60	Ib	6.0	Ib	5.0	Ib	3.6	Ib	4.0
80	Ib	7.3	Ib	6.2	Pair-unstable	–	Pair-unstable	–
120	Ib	6.0	Pair-unstable	–	Pair-unstable	–	Pair-unstable	–

Table 12. Dust masses produced by ROT calibrated-energy models (CE) of different metallicity: CE0 ([Fe/H] = 0), CE-1 ([Fe/H] = −1), CE-2 ([Fe/H] = −2), CE-3 ([Fe/H] = −3). Progenitor mass (M), SN type, and dust mass ($M_{\rm dust}$). We also indicate the pair unstable models for which dust formation has not been computed.

	CE ROT							
	CE0		CE-1		CE-2		CE-3	
M ($M_\odot$)	SN-type	$M_{\rm dust}$ ($M_\odot$)	SN-type	$M_{\rm dust}$ ($M_\odot$)	SN-type	$M_{\rm dust}$ ($M_\odot$)	SN-type	$M_{\rm dust}$ ($M_\odot$)
13	Ib	0.65	II-P	0.49	II-P	0.49	II-P	0.72
15	Ib	1.5	II-P	0.56	II-P	0.73	II-P	0.93
20	Ib	1.2	II-P	1.4	II-P	1.1	II-P	0.96
25	Ib	1.1	II-P	1.8	Ib	1.2	Ib	1.1
30	Ib	1.4	Ib	1.6	Ib	1.4	Ib	1.9
40	Ib	2.0	Ib	2.8	Ib	3.3	Ib	3.4
60	Ib	3.2	Ib	4.8	Ib	7.4	Ib	6.6
80	Ib	3.4	Ib	5.6	Pair-unstable	–	Pair-unstable	–
120	Ib	3.8	Pair-unstable	–	Pair-unstable	–	Pair-unstable	–

This paper has been typeset from a TEX/LATEX file prepared by the author.